






Article

Constructing g-C₃N₄/Cd_{1-x}Zn_xS-Based Heterostructures for Efficient Hydrogen Production under Visible Light

Angelina V. Zhurenok ¹, Dina V. Markovskaya ¹, Evgeny Y. Gerasimov ¹ , Alexander S. Vokhmintsev ² , Ilya A. Weinstein ^{2,3} , Igor P. Prosvirin ¹, Svetlana V. Cherepanova ¹, Andrey V. Bukhtiyarov ¹  and Ekaterina A. Kozlova ^{1,*} 

¹ Federal Research Center Boreskov Institute of Catalysis, Pr. Ak. Lavrentieva, 5, 630090 Novosibirsk, Russia; angelinazhurenok@gmail.com (A.V.Z.); madiva@catalysis.ru (D.V.M.); gerasimov@catalysis.ru (E.Y.G.); prosvirin@catalysis.ru (I.P.P.); svch@catalysis.ru (S.V.C.); avb@catalysis.ru (A.V.B.)

² NANOTECH Centre, Ural Federal University, St. Mira, 19, 620002 Ekaterinburg, Russia; a.s.vokhmintsev@urfu.ru (A.S.V.); i.a.weinstein@urfu.ru (I.A.W.)

³ Institute of Metallurgy of the Ural Branch of the Russian Academy of Sciences, 620016 Ekaterinburg, Russia

* Correspondence: kozlova@catalysis.ru; Tel.: +7-383-326-95-43



Citation: Zhurenok, A.V.; Markovskaya, D.V.; Gerasimov, E.Y.; Vokhmintsev, A.S.; Weinstein, I.A.; Prosvirin, I.P.; Cherepanova, S.V.; Bukhtiyarov, A.V.; Kozlova, E.A. Constructing g-C₃N₄/Cd_{1-x}Zn_xS-Based Heterostructures for Efficient Hydrogen Production under Visible Light. *Catalysts* **2021**, *11*, 1340. <https://doi.org/10.3390/catal11111340>

Academic Editors: Ki Tae Park, Chang-Tang Chang and Wonhee Lee

Received: 17 October 2021

Accepted: 4 November 2021

Published: 6 November 2021

Publisher's Note: MDPI stays neutral with regard to jurisdictional claims in published maps and institutional affiliations.



Copyright: © 2021 by the authors. Licensee MDPI, Basel, Switzerland. This article is an open access article distributed under the terms and conditions of the Creative Commons Attribution (CC BY) license (<https://creativecommons.org/licenses/by/4.0/>).

Abstract: Two types of photocatalysts, 1%Pt/Cd_{1-x}Zn_xS/g-C₃N₄ (x = 0.2–0.3) and Cd_{1-x}Zn_xS/1%Pt/g-C₃N₄ (x = 0.2–0.3), were synthesized by varying the deposition order of platinum, and a solid solution of cadmium and zinc sulfides onto the surface of g-C₃N₄. The characterization of photocatalysts showed that, for 1%Pt/Cd_{1-x}Zn_xS/g-C₃N₄, small platinum particles were deposited onto a solid solution of cadmium and zinc sulfides; in the case of Cd_{1-x}Zn_xS/1%Pt/g-C₃N₄, enlarged platinum clusters were located on the surface of graphitic carbon nitride. Based on the structure of the photocatalysts, we assumed that, in the first case, type II heterojunctions and, in the latter case, S-scheme heterojunctions were realized. The activity of the synthesized samples was tested in hydrogen evolution from triethanolamine (TEOA) basic solution under visible light (λ = 450 nm). A remarkable increase in hydrogen evolution rate compared to single-phase platinized 1%Pt/Cd_{1-x}Zn_xS photocatalysts was observed only in the case of ternary photocatalysts with platinum located on the g-C₃N₄ surface, Cd_{1-x}Zn_xS/1%Pt/g-C₃N₄. Thus, we proved using kinetic experiments and characterization techniques that, for composite photocatalysts based on Cd_{1-x}Zn_xS and g-C₃N₄, the formation of the S-scheme mechanism is more favorable than that for type II heterojunction. The highest activity, 2.5 mmol H₂ g⁻¹ h⁻¹, with an apparent quantum efficiency equal to 6.0% at a wavelength of 450 nm was achieved by sample 20% Cd_{0.8}Zn_{0.2}S/1% Pt/g-C₃N₄.

Keywords: solar energy; photocatalytic hydrogen evolution; visible light; g-C₃N₄

1. Introduction

The main trend in the reduction in readily available high-quality carbon-containing fossil fuels is the urgent need for the development of available alternative-energy sources, particularly renewable energy. One of the most promising future energy directions may be solar energy. Thus, the total amount of solar energy reaching Earth is 3×10^{24} J/year, which is about 10,000 times the current total global energy consumption [1]. Photoinduced hydrogen production from water and aqueous solutions of inorganic and organic compounds is the subject of investigations due to the possibility of direct conversion of solar energy to chemical-bond energy. Works searching for efficient semiconductor photocatalysts for water splitting and hydrogen production under light irradiation have been actively carried out since the 1980s, when the pioneering work of Fujishima and Honda was published [2].

A new impetus to the development of methods for the synthesis of materials for photocatalytic water splitting and hydrogen production was given by the discovery of a previously unknown photocatalyst: polymer graphitic carbon nitride g-C₃N₄ [3]. This material possesses the properties of a semiconductor with a band gap of 2.7 eV (λ = 460 nm),

a position of valence band (VB) levels of +1.6 V vs. NHE, and conduction bands (CB) levels of −1.1 V vs. NHE [4]. The latter value is one of the most negative for known semiconductor photocatalysts and favors the process of water reduction. In addition, g-C₃N₄ is stable in both acidic and alkaline media and at thermal treatments up to 700 °C and may be synthesized from available nitrogen-containing organics such as cyanamides, melamine, and urea. These properties make g-C₃N₄ an ideal semiconductor for photocatalytic hydrogen production, CO₂ reduction, and solar-cell applications [5–7]. However, quantum efficiency in the photocatalytic hydrogen production over pristine g-C₃N₄ is quite low [8].

The main problem in photocatalytic hydrogen production is a recombination of electron-hole pairs in bulk or on the semiconductor surface [9–11]. The quantum efficiency of photocatalytic hydrogen evolution may be sufficiently increased while ensuring the separation of photogenerated charges in space [12]. For this purpose, composite semiconductor materials that provide the stimulated spatial separation of photogenerated charges are formed. For example, this can be performed by creating heterojunctions that ensure the transfer of charge carriers across the semiconductor 1/semiconductor 2 interface [13–15]. For these systems, multiple pathways for photoinduced electron and hole migration may be realized [16,17]. Recently, composite systems such as CdS/g-C₃N₄ [14], TiO₂/g-C₃N₄ [15], BiVO₄/g-C₃N₄ [18], and CoO/g-C₃N₄ [19] have been proposed for photocatalytic hydrogen production. Photocatalysts based on g-C₃N₄ and CdS or Cd_{1−x}Zn_xS are considered very promising materials for the photocatalytic production of hydrogen [14,20–25], CO₂ reduction, [5], and the oxidation of various organic substances [26,27], because both CdS or Cd_{1−x}Zn_xS and g-C₃N₄ absorb visible light and have suitable VB and CB positions to form interfacial heterojunctions. Additionally, these composite materials can be obtained from cheap antecedents using simple synthetic techniques. The solid solution of cadmium and zinc sulfides is a preferable component of the composite as compared to pristine cadmium sulfide since, in the first case, the positions of the flat bands of the Cd_{1−x}Zn_xS solid solution can be adjusted [28].

In general, heterojunctions for systems based on g-C₃N₄ and Cd_{1−x}Zn_xS could be divided into three main categories, namely, type II, Z-scheme, and S-scheme heterojunctions [29–32]. For systems with a conventional type II heterojunction, the separation of photogenerated charges can be achieved. However, according to the heterojunction formation mechanism, in this case, the photogenerated electrons move from the CB of g-C₃N₄ to the CB of the semiconductor with the less negative CB position, e.g., Cd_{1−x}Zn_xS. This results in a decrease in the reduction ability of photogenerated electrons and therefore the quantum efficiency of hydrogen production [5,33]. From a practical point of view, achieving efficient charge separation while maintaining high redox abilities is a challenge for constructing g-C₃N₄-based photocatalysts [34,35]. Creating photocatalysts with both Z-scheme and S-scheme heterojunctions is considered an efficient method of improving the photocatalytic activity of g-C₃N₄, because in this case, electrons remain in the CB of g-C₃N₄, and therefore retain their high reduction ability [32,33]. Recently, Zn_xCd_{1−x}S/Au/g-C₃N₄ ternary composites with a Z-scheme heterojunction with enhanced activity in hydrogen evolution and CO₂ reduction have been reported [5,20,21]. However, it has recently been shown that for ternary photocatalysts like Zn_xCd_{1−x}S/Au/g-C₃N₄, all-solid-state Z-schemes cannot be used as according to the analysis of work function and interface Fermi level balance, because formed Schottky heterojunctions will prevent the transfer of electron in two semiconductors; thus, the probability of S-scheme formation between Zn_xCd_{1−x}S and g-C₃N₄ is higher [32,36].

At the same time, systems of a similar kind with platinum as a cocatalyst have not been reported as Z-scheme or S-scheme, although platinum is recognized as the most efficient cocatalyst for hydrogen production due to its high work function [9,37,38]. Only a conventional type II heterojunction has been described for ternary Pt/CdS/g-C₃N₄ composites [22–25,27]. The authors of these works suggested that photogenerated electrons pass into the conduction band of CdS and then transfer to platinum nanoparticles, which act as a cocatalyst for the formation of hydrogen [22–25]. To the best of our knowledge,

ternary Pt/CdS/g-C₃N₄ and Pt/Cd_{1-x}Zn_xS/g-C₃N₄ systems have not been considered as Z-scheme or S-scheme heterojunction photocatalysts.

In this work, we compared two types of photocatalysts with platinum nanoparticles deposited on the surface of g-C₃N₄ (Cd_{1-x}Zn_xS/Pt/g-C₃N₄), and those with platinum nanoparticles deposited on the surface of a Cd_{1-x}Zn_xS solid solution (Pt/Cd_{1-x}Zn_xS/g-C₃N₄). Thus, we aimed to understand the probable role of platinum and the mechanism of the formation of the heterojunctions for Cd_{1-x}Zn_xS/g-C₃N₄-based systems. The synthesis of Cd_{1-x}Zn_xS/g-C₃N₄ with the different locations of platinum particles and the assessment of their photocatalytic properties was carried out for the first time. The experiments clearly showed that photocatalysts of the Cd_{1-x}Zn_xS/Pt/g-C₃N₄ type possessed significantly higher activity in comparison to that of Pt/Cd_{1-x}Zn_xS/g-C₃N₄ photocatalysts, suggesting that the occurrence of the S-scheme is more favorable for the photocatalytic production of hydrogen.

2. Results

2.1. Characterization of Photocatalysts Based on Cd_{1-x}Zn_xS/g-C₃N₄

We obtained two types of photocatalysts, 1%Pt/Cd_{1-x}Zn_xS/g-C₃N₄ (x = 0.2–0.3) and Cd_{1-x}Zn_xS/1%Pt/g-C₃N₄ (x = 0.2–0.3), by varying the deposition order of platinum and a solid solution of cadmium and zinc sulfides onto the surface of g-C₃N₄. For Scheme 1 (Table 1), first, Cd_{1-x}Zn_xS was deposited on the surface of g-C₃N₄, followed by metal deposition on the composite surface. In the case of Scheme 2 (Table 1), Cd_{1-x}Zn_xS was deposited on the surface of pre-platinized Pt/g-C₃N₄. The abbreviation and properties of all synthesized samples are listed in Table 1; the X-ray diffraction patterns of the photocatalysts are shown in Figure 1.

Table 1. Abbreviations and activity of the synthesized photocatalysts in hydrogen production. Conditions: C₀(NaOH) = 0.1 M, C₀(TEOA) = 10 vol%, C_{cat} = 0.5 g L⁻¹; LED light source (λ = 450 nm).

Photocatalyst	Composition	W(H ₂), μmol min ⁻¹	Activity, μmol g ⁻¹ h ⁻¹	AQE, %
Cd0.8	Cd _{0.8} Zn _{0.2} S	<0.01	<10	<0.3
Cd0.7	Cd _{0.7} Zn _{0.3} S	<0.01	<10	<0.3
CN	g-C ₃ N ₄	0	0	0
Pt/Cd0.8	1%Pt/Cd _{0.8} Zn _{0.2} S	1.10	1310	3.2
Pt/Cd0.7	1%Pt/Cd _{0.7} Zn _{0.3} S	0.57	684	1.7
Pt/CN	1%Pt/g-C ₃ N ₄	0.37	444	1.1
Composite samples without Pt				
10Cd0.8/CN	10 wt% Cd _{0.8} Zn _{0.2} S/g-C ₃ N ₄	0.08	96	0.24
20Cd0.8/CN	20 wt% Cd _{0.8} Zn _{0.2} S/g-C ₃ N ₄	0.13	156	0.38
50Cd0.8/CN	50 wt% Cd _{0.8} Zn _{0.2} S/g-C ₃ N ₄	0.10	120	0.29
10Cd0.7/CN	10 wt% Cd _{0.7} Zn _{0.3} S/g-C ₃ N ₄	0.09	108	0.26
20Cd0.7/CN	20 wt% Cd _{0.7} Zn _{0.3} S/g-C ₃ N ₄	0.07	84	0.21
50Cd0.7/CN	50 wt% Cd _{0.7} Zn _{0.3} S/g-C ₃ N ₄	0.09	108	0.26
Scheme 1 (Pt-sulfide-nitride)				
Pt/10Cd0.8/CN	1%Pt/10 wt% Cd _{0.8} Zn _{0.2} S/g-C ₃ N ₄	0.19	228	0.56
Pt/20Cd0.8/CN	1%Pt/20 wt% Cd _{0.8} Zn _{0.2} S/g-C ₃ N ₄	0.83	996	2.4
Pt/50Cd0.8/CN	1%Pt/50 wt% Cd _{0.8} Zn _{0.2} S/g-C ₃ N ₄	0.80	960	2.4
Pt/10Cd0.7/CN	1%Pt/10 wt% Cd _{0.7} Zn _{0.3} S/g-C ₃ N ₄	0.19	228	0.56
Pt/20Cd0.7/CN	1%Pt/20 wt% Cd _{0.7} Zn _{0.3} S/g-C ₃ N ₄	0.41	492	1.2
Pt/50Cd0.7/CN	1%Pt/50 wt% Cd _{0.7} Zn _{0.3} S/g-C ₃ N ₄	0.60	708	1.8
Scheme 2 (sulfide-Pt-nitride)				
10Cd0.8/Pt/CN	10 wt% Cd _{0.8} Zn _{0.2} S/1%Pt/g-C ₃ N ₄	1.50	1800	4.4
20Cd0.8/Pt/CN	20 wt% Cd _{0.8} Zn _{0.2} S/1%Pt/g-C ₃ N ₄	2.10	2520	6.2
50Cd0.8/Pt/CN	50 wt% Cd _{0.8} Zn _{0.2} S/1%Pt/g-C ₃ N ₄	1.60	1920	4.7
10Cd0.7/Pt/CN	10 wt% Cd _{0.7} Zn _{0.3} S/1%Pt/g-C ₃ N ₄	1.50	1800	4.4
20Cd0.7/Pt/CN	20 wt% Cd _{0.7} Zn _{0.3} S/1%Pt/g-C ₃ N ₄	1.90	2280	5.6
50Cd0.7/Pt/CN	50 wt% Cd _{0.7} Zn _{0.3} S/1%Pt/g-C ₃ N ₄	1.66	1990	4.9

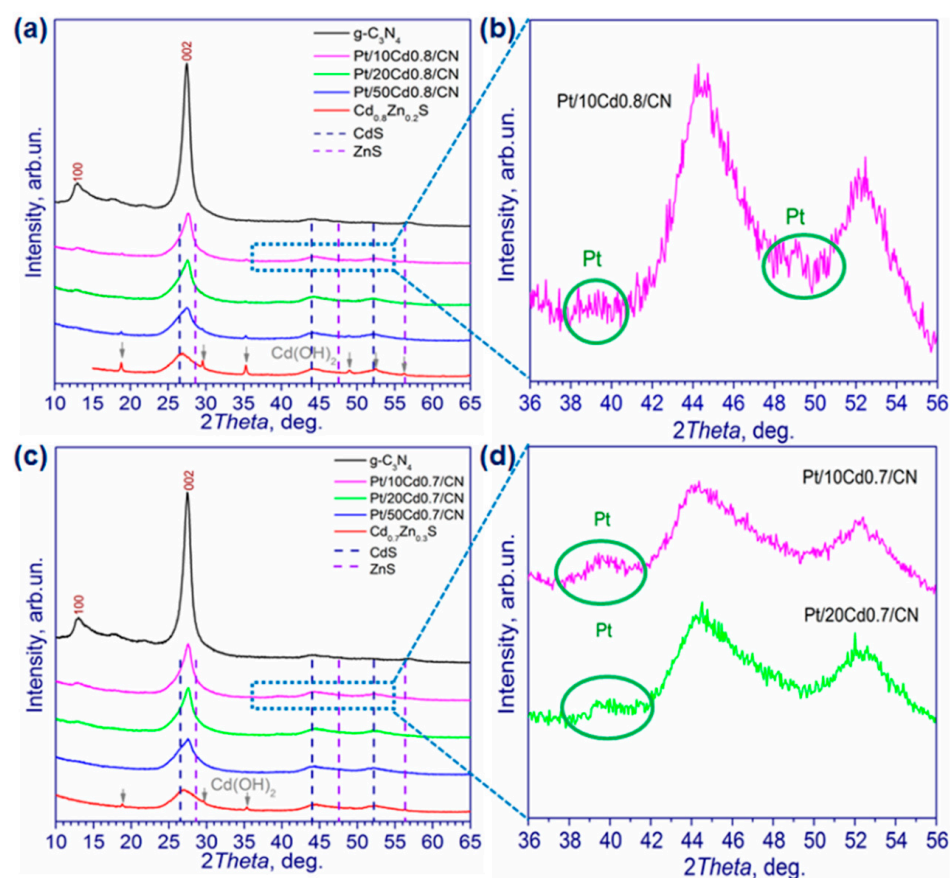


Figure 1. XRD patterns of the photocatalysts based on Cd_{0.8}Zn_{0.2}S/g-C₃N₄ (a,b) and Cd_{0.7}Zn_{0.3}S/g-C₃N₄ (c,d).

The pristine g-C₃N₄ had clear diffraction peaks at 13.0° and 27.5°, which corresponded to the (100) and (002) planes of graphitic carbon nitride [39,40]. The first peak was attributed to in-plane repeated units of tri-s-triazine, whereas the second was related to the interlayer packing of g-C₃N₄ with the (002) diffraction plane [5]. Pristine Cd_{0.8}Zn_{0.2}S (Figure 1a) and Cd_{0.7}Zn_{0.3}S (Figure 1c) had three broad diffraction peaks located at 26.8–27.0°, 44.2–44.4°, and 50.0–52.3°, which corresponded to the (111), (220), and (311) planes, respectively, of the Cd_{1-x}Zn_xS ($x = 0.2$ – 0.3) solid solutions with a cubic structure. Impure Cd(OH)₂ peaks were also observed for the samples with Cd_{0.8}Zn_{0.2}S and Cd_{0.7}Zn_{0.3}S. The XRD patterns of composite photocatalysts Cd_{0.8}Zn_{0.2}S/g-C₃N₄ and Cd_{0.7}Zn_{0.3}S/g-C₃N₄ contained diffraction peaks of both g-C₃N₄ and Cd_{1-x}Zn_xS solid solutions. The relative intensity of the (002) peak decreased with the increase in solid solution content. In the ternary composites (Pt/Cd_{0.8}/CN and Pt/Cd_{0.7}/CN), very low peaks of platinum were observed at $2\Theta = 40^\circ$ and ca. 46° , and average particle size ca. 2 nm. The average crystallite sizes of g-C₃N₄ calculated from diffraction peaks (100) and (002) were 11.7 nm in the plane of the layers and 19.8 nm in the direction perpendicular to the layers, respectively, for all samples and did not change after the deposition of Cd_{1-x}Zn_xS. The average crystalline size values for Cd_{1-x}Zn_xS varied within 7.4–9.6 nm ($x = 0.2$) and 5.1–8.5 nm ($x = 0.3$). The crystalline size grew with the increase in the amount of the corresponding solid solution of CdS and ZnS; for pristine Cd_{0.8}Zn_{0.2}S and Cd_{0.7}Zn_{0.3}S, these values were 7.3 and 5.7 nm, respectively. The deposition order of the photocatalyst component was not significantly implied by the XRD patterns and values of average crystallite size.

The textural properties of the photocatalysts were also investigated (Table 2). The specific surface area of pristine Cd_{0.8}Zn_{0.2}S was equal to 177 m² g⁻¹, whereas the surface area of g-C₃N₄ did not exceed 20 m² g⁻¹. The formation of the hybrid composite structure

led to an intermediate specific surface area from 34 to 68 m² g^{−1}, wherein the surface increased with the content of the Cd_{0.8}Zn_{0.2}S solid solution in the composite.

Table 2. Textural and optical properties of the ternary composite photocatalysts, Cd_{0.8}Zn_{0.2}S, and g-C₃N₄ samples.

Photocatalyst	Average Crystallite Size of Cd _{1-x} Zn _x S, nm	S _{BET} , m ² g ^{−1}	Pore Volume, cm ³ g ^{−1}	Band Gap, eV
Cd _{0.8} (Cd _{0.8} Zn _{0.2} S)	7.3	177	0.20	2.37
CN (g-C ₃ N ₄)	–	19	0.12	2.85
Pt/10Cd _{0.8} /CN	7.4	34	0.13	2.81
Pt/20Cd _{0.8} /CN	8.0	37	0.13	2.79
Pt/50Cd _{0.8} /CN	9.6	68	0.14	2.75

UV–visible spectra of the g-C₃N₄, Cd_{0.8}Zn_{0.2}S photocatalysts, and ternary composites were obtained, and the result is shown in Figure 2a,b. The spectra of the composite samples lay between the UV–vis spectra of the g-C₃N₄ and Cd_{0.8}Zn_{0.2}S samples. Platinum nanoparticles also decreased reflectance in the range of 500–800 nm. The absorption edges of the composite samples and Cd_{0.8}Zn_{0.2}S were estimated using the Tauc function for semiconductors with direct transitions, $F(R)^2(h\nu)^2$ (Figure 2c,d). For g-C₃N₄, the band gap was 2.85 eV (absorption edge was 435 nm); for Cd_{0.8}Zn_{0.2}S, the band gap was 2.37 eV (absorption edge was 523 nm); and the adsorption edges of the composite ternary samples had intermediate values (Table 2). The absorption edges of two series of photocatalysts, Pt/Cd_{0.8}/CN (Scheme 1) and Cd_{0.8}/Pt/CN (Scheme 2), were close to each other, and the spectra had no remarkable differences. Altogether, all prepared samples absorbed visible light and could be used as active photocatalysts for hydrogen photoproduction.

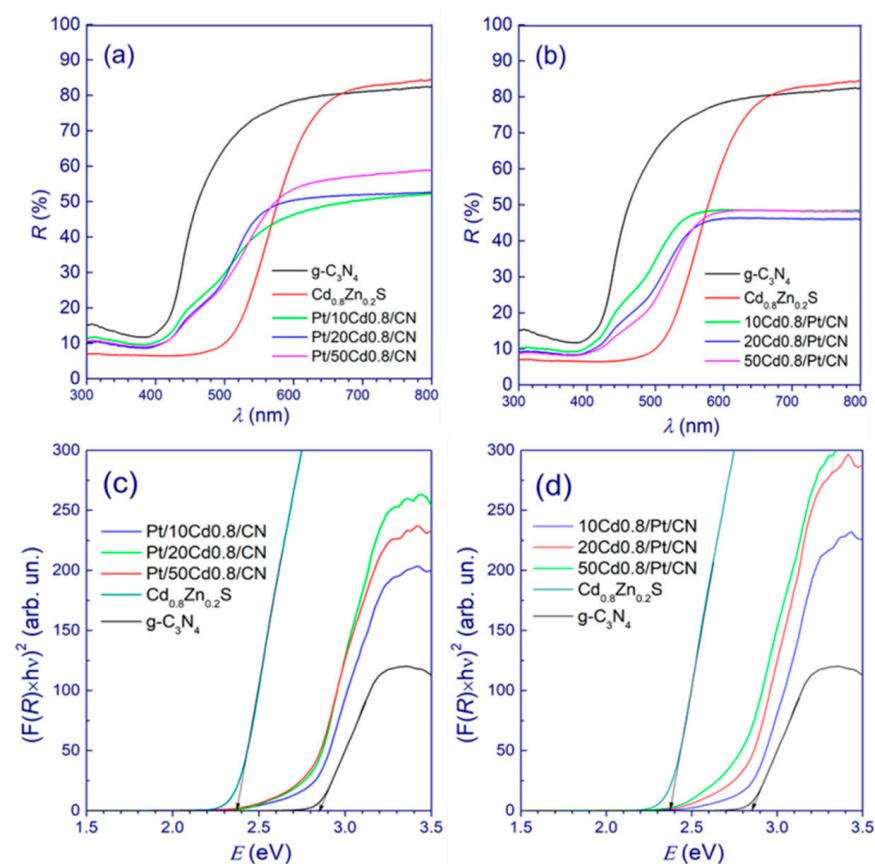


Figure 2. Diffuse reflectance spectra (a,b) and Tauc plot (c,d) for the samples Cd_{0.8}Zn_{0.2}S, g-C₃N₄, Pt/Cd_{0.8}/CN (Scheme 1) (a,c), and Cd_{0.8}/Pt/CN (Scheme 2) (b,d).

The XPS method was used to study the Pt/20Cd_{0.8}/CN and 20Cd_{0.8}/Pt/CN samples prepared according to Schemes 1 and 2, respectively (Figure 3). The survey spectra showed

the presence of C, S, N, and Pt elements on the surface of ternary composites. Figure 3a shows that C1s had two peaks with binding energies of 284.8 and 288.1 eV corresponding to the C–C and N–C=N bonds in g-C₃N₄, respectively [41]. The first peak may be attributed to the adventitious carbon [42]. For the 20Cd0.8/Pt/CN sample, the peak corresponding to the C–C bond was higher than that for Pt/20Cd0.8/CN, and the peak corresponding to the N–C=N bond was lower. The N1s XPS peak (Figure 3b) could be divided into three peaks located at 404.9, 400.0, and 398.9 eV. The main peak at 398.9 eV came from sp²-bonded nitrogen, which was included in the triazine rings C=N–C of g-C₃N₄, the peak at 400.4 eV was related to the N–(C)₃ bond, and the peak at 404.9 eV was probably linked to the C–N–H bond [43]. The S2p peaks (Figure 3c) around 161.4 indicate that the state of sulfur is S^{2−} [44]. Sulfur is partially oxidized in air to SO₃^{2−} or SO₄^{2−}, confirmed by the peak at 168.0 eV [45]. The content of oxidized forms of sulfur was quite low for both samples. The Pt4f peaks at 71.1 and 72.5 eV correspond to two states of platinum, Pt⁰ and Pt²⁺ (Figure 3d) [46,47].

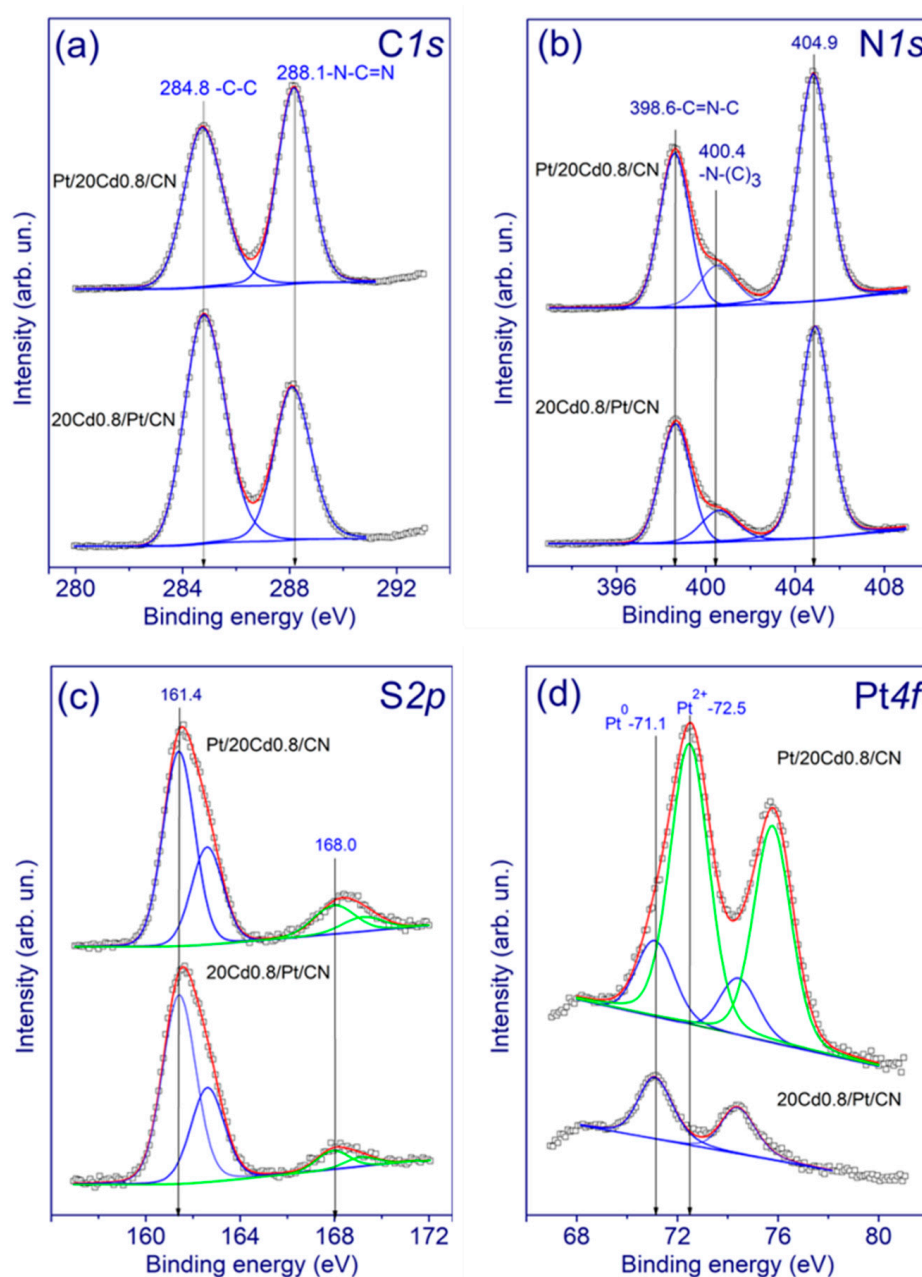


Figure 3. The C1s (a), N1s (b), S2p (c), and Pt4f (d) XPS spectra of the photocatalysts Pt/20Cd0.8/CN and 20Cd0.8/Pt/CN.

Table 3 represents the surface ratios of elements calculated using the XPS technique. The main difference is the surface content of platinum. In the case of Scheme 1, when platinum was deposited onto the surface of the $\text{Cd}_{0.8}\text{Zn}_{0.2}\text{S}/\text{g-C}_3\text{N}_4$ composite, the surface ratio $[\text{Pt}]/[\text{Cd} + \text{Zn}]$ was six times higher than that in the case of platinum deposition onto the surface of $\text{g-C}_3\text{N}_4$ nitride, followed by sulfide solid solution deposition (Scheme 2), at the same Pt loading, 1 wt. %, which looked quite logical from the synthesis technique, because in the case of Scheme 2, a solid solution of cadmium and zinc sulfides is deposited over the platinum located on the surface of $\text{g-C}_3\text{N}_4$, which can reduce the surface concentration of platinum. Additionally, later in the text, it will be shown by the TEM method that in the case of Scheme 1, smaller platinum particles are formed. For the $20\text{Cd}0.8/\text{Pt}/\text{CN}$ sample, Pt existed only in metallic form, while Pt^0 and Pt^{2+} were identified for $\text{Pt}/20\text{Cd}0.8/\text{CN}$. For the sample prepared according to Scheme 2, $20\text{Cd}0.8/\text{Pt}/\text{CN}$, the percentage of sulfur in the form of sulfide was higher at 92% compared to 84% in the case of photocatalyst $\text{Pt}/20\text{Cd}0.8/\text{CN}$. For $\text{Pt}/\text{Cd}_{1-x}\text{Zn}_x\text{S}$ photocatalysts, platinum in metallic state and sulfur in S^{2-} state are preferable for photocatalytic hydrogen production [48].

Table 3. Surface properties of the photocatalysts $\text{Pt}/20\text{Cd}0.8/\text{CN}$ and $20\text{Cd}0.8/\text{Pt}/\text{CN}$ before and after the photocatalytic hydrogen production based on XPS data.

Photocatalyst	$[\text{Cd} + \text{Zn}]/[\text{C}]$	$[\text{S}]/[\text{C}]$	$[\text{Pt}]/[\text{C}]$	$[\text{Pt}]/[\text{Cd} + \text{Zn}]$	Pt State, %		S State, %	
					Pt^0	Pt^{2+}	S^{2-}	SO_x^{2-}
$\text{Pt}/20\text{Cd}0.8/\text{CN}$	0.14	0.13	0.0045	0.031	21	79	84	16
$\text{Pt}/20\text{Cd}0.8/\text{CN}^*$	0.05	0.04	0.0036	0.070	40	60	100	0
$20\text{Cd}0.8/\text{Pt}/\text{CN}$	0.11	0.10	0.0006	0.005	100	0	92	8
$20\text{Cd}0.8/\text{Pt}/\text{CN}^*$	0.07	0.06	0.0018	0.024	74	26	100	0

* after photocatalytic tests.

The composition of the $\text{Pt}/20\text{Cd}0.8/\text{CN}$ photocatalyst (Scheme 1) was studied with the HAADF-STEM method with EDX elemental mapping. Figure 4 confirms the presence of Cd, Zn, Pt, C, N, and S in the tested sample. Figure 4a,f demonstrate the formation of C_3N_4 material, whereas Figure 4b–d reveal the presence of the $\text{Cd}_{1-x}\text{Zn}_x\text{S}$ phase. It was important to define the location of Pt nanoparticles in the sample. The comparison of Figure 4b–d proves the platinization of the $\text{Cd}_{1-x}\text{Zn}_x\text{S}$ phase only because no platinum signal was observed in the absence of Cd, S, and Zn. Figure 4g–i show that Pt nanoparticles were uniformly distributed on the surface of the solid solution; Pt particle size did not exceed 2 nm.

The $20\text{Cd}0.8/\text{Pt}/\text{CN}$ sample was studied by the HRTEM method. Figure 5a demonstrates the formation of two particle types in the samples. The first was connected with the layer structure identifying $\text{g-C}_3\text{N}_4$. The domains with regular structure and sizes at about 10–15 nm may be attributed to the solid solution of CdS and ZnS. The particle sizes were slightly higher than the calculated average crystallite sizes. Therefore, the XRD and HRTEM data coincided with each other. Figure 5a also demonstrates good interphase contact between $\text{Cd}_{1-x}\text{Zn}_x\text{S}$ and C_3N_4 and confirms the possibility of heterojunction formation. The $20\text{Cd}0.8/\text{Pt}/\text{CN}$ photocatalyst was also investigated by the HAADF-STEM method with EDX elemental mapping. Figure 5c–f show the elemental distribution in the $20\text{Cd}0.8/\text{Pt}/\text{CN}$ sample. Figure 5e,f define the location of the Pt cocatalyst: large elongated clusters of platinum particles were located over the surface of $\text{g-C}_3\text{N}_4$; the length of some clusters particles reached 100 nm. The platinum clusters are shown in Figure 5b; one can see that these clusters consisted of Pt nanoparticles with a size of 2–5 nm. The formation of clusters can be explained by the inhomogeneity of the surface of layered graphitic carbon nitride, on which the platinum particles were deposited. It has recently been shown that this kind of noble metal cluster can be an effective cocatalyst for the photocatalytic process [49]. To elucidate the location of the platinum, we summarized the EDX local analysis data in Tables S1–S4 (Supplementary Materials). EDX data confirm that platinum nanoparticles with a high concentration (1.3–1.7 at. %) are localized in domains

with a dominant content of g-C₃N₄. For areas where both sulfide and nitride are found, the platinum concentration does not exceed 0.2 at. %.

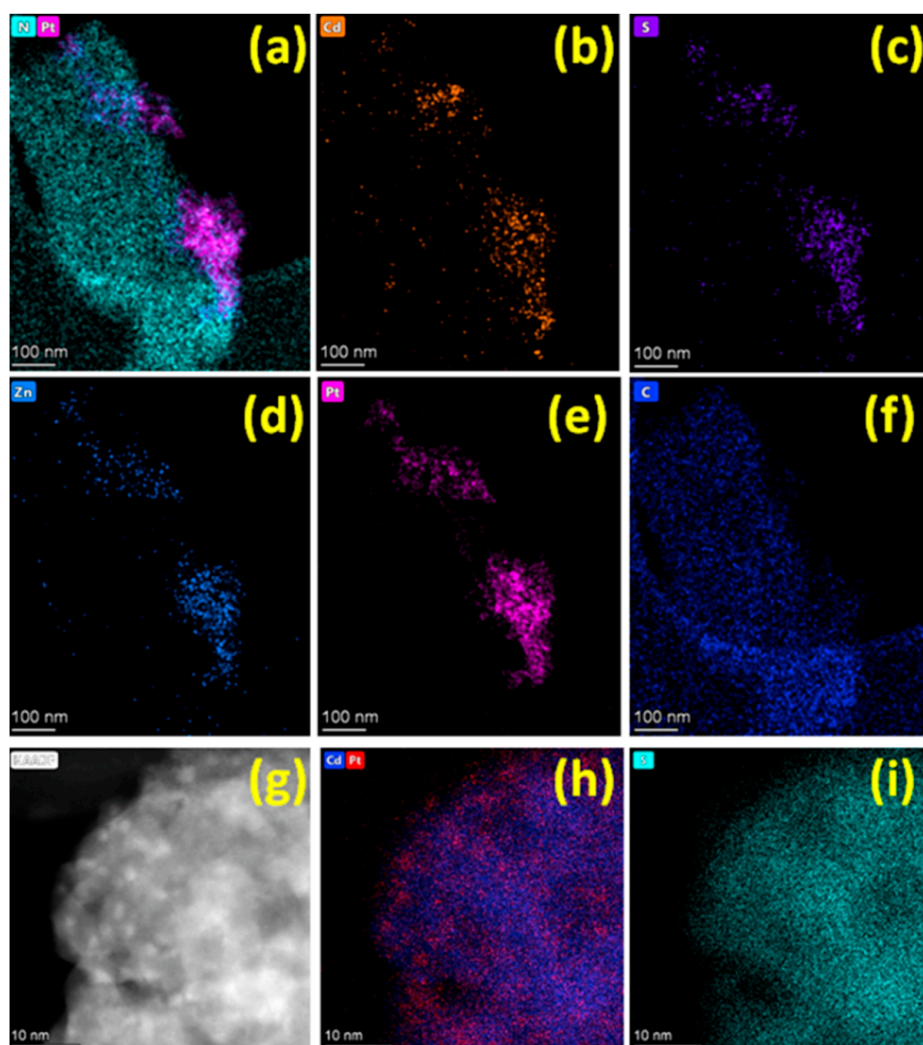


Figure 4. Elemental mapping (a–f,h,i) and HAADF STEM (g) of the photocatalyst Pt/20Cd0.8/CN.

TEM analysis suggests that the Pt/20Cd0.8/CN (Scheme 1) and 20Cd0.8/Pt/CN (Scheme 2) photocatalysts had fundamentally different structures: in the first case, small platinum particles were deposited onto a surface of the solid solution of cadmium and zinc sulfides in the Cd_{0.8}Zn_{0.2}S/g-C₃N₄ composite; in the latter case, enlarged platinum clusters were located on the surface of graphitic carbon nitride. A similar structure was also confirmed by XPS data, since in the second case, the surface content of platinum was much lower. In addition, according to XPS data, in the first case, platinum was present in oxidation states Pt⁰ and Pt²⁺, while in the latter, it was only metallic state Pt⁰.

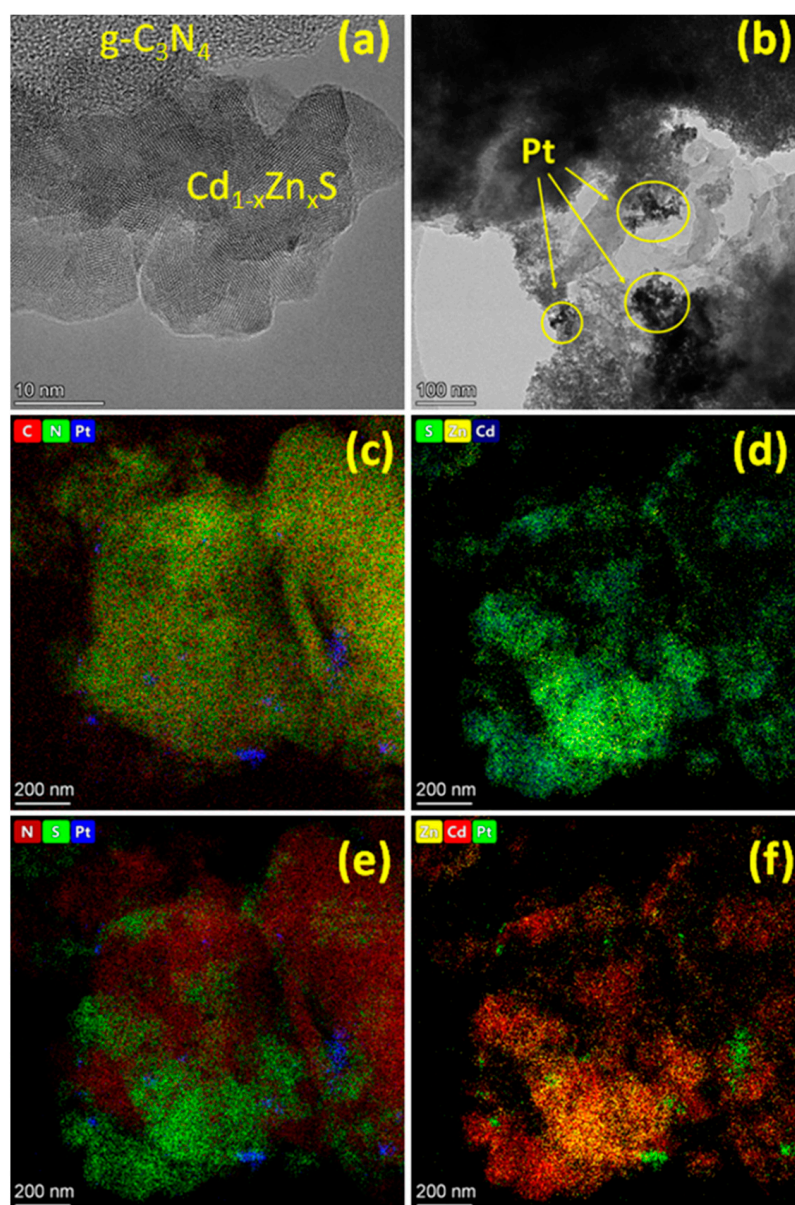


Figure 5. HRTEM images (a,b) and elemental mapping of (c–f) of the photocatalyst 20Cd0.8/Pt/CN.

2.2. Photocatalytic Tests

Photocatalytic hydrogen evolution from aqueous solutions of TEOA was investigated under visible light irradiation ($\lambda = 450$ nm). To facilitate the proton abstraction during the chain process of TEOA oxidation and therefore to prevent charge recombination the reaction was carried out in an 0.1 M NaOH aqueous solution [50]. The kinetics of hydrogen evolution over the selected photocatalysts is shown in Figure 6a. For pristine g-C₃N₄, Cd_{0.8}Zn_{0.2}S, and Cd_{0.7}Zn_{0.3}S, the hydrogen evolution rate was close to zero. The rates of hydrogen production over samples 10–50 Cd0.8/CN and 10–50 Cd0.7/CN are shown in Figure 6b. For the photocatalysts without platinum, the rate of hydrogen formation did not exceed 0.13 μmol hydrogen per minute. Considering that the rates of hydrogen production in the presence of g-C₃N₄, or Cd_{0.8}Zn_{0.2}S and Cd_{0.7}Zn_{0.3}S solid solutions were close to zero, the creation of composite samples led to a remarkable increase in activity in comparison to the pristine compounds, confirming the appearance of interphase heterojunctions between g-C₃N₄ and Cd_{1-x}Zn_xS.

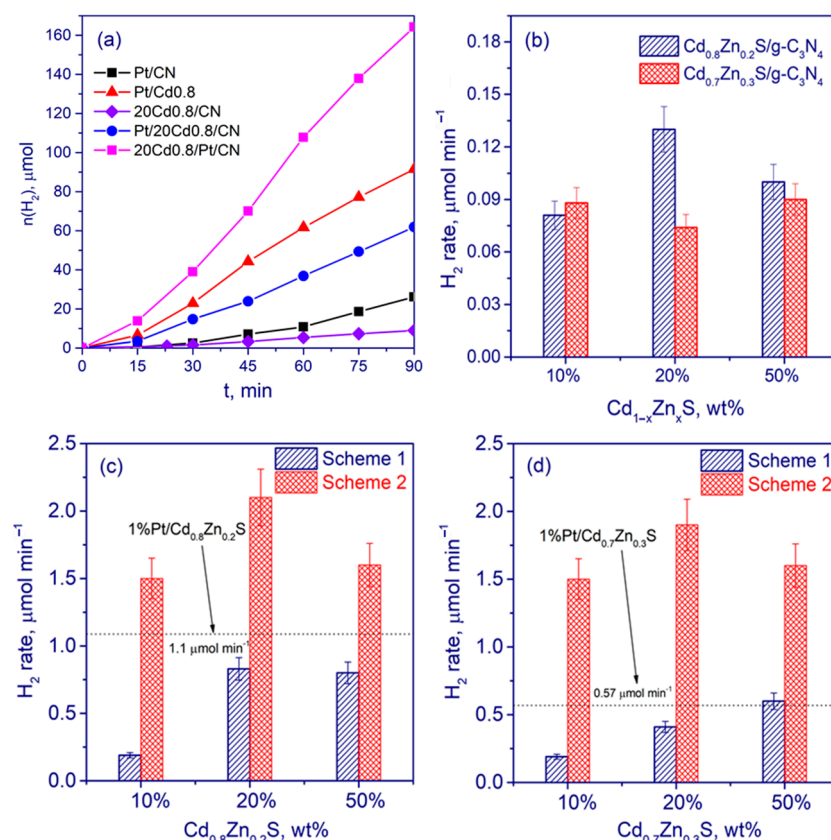


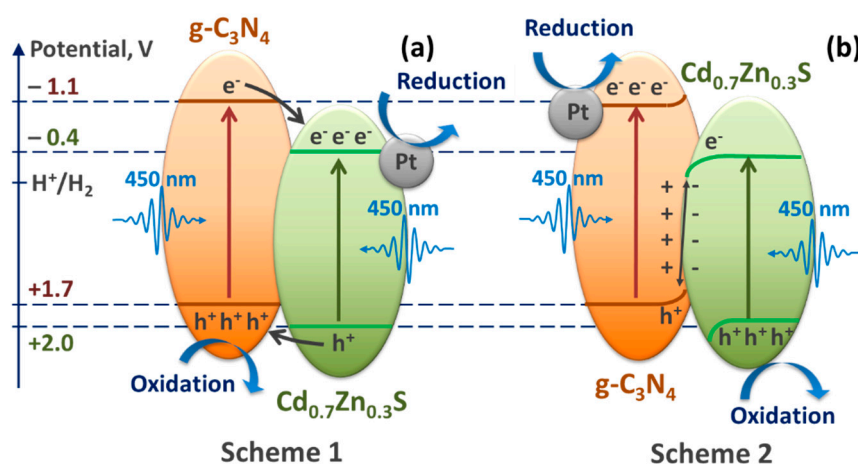
Figure 6. Kinetic curves of the photocatalytic hydrogen evolution over selected photocatalysts (a); comparative data on hydrogen production over composite photocatalysts $\text{Cd}_{1-x}\text{Zn}_x\text{S}/\text{g-C}_3\text{N}_4$ ($x = 0.2-0.3$) (b) and ternary systems 1%Pt/ $\text{Cd}_{1-x}\text{Zn}_x\text{S}/\text{g-C}_3\text{N}_4$ (Scheme 1) or $\text{Cd}_{1-x}\text{Zn}_x\text{S}/1\%\text{Pt}/\text{g-C}_3\text{N}_4$ (Scheme 2) ($x = 0.2$) (c); $x = 0.3$) (d). Conditions: $C_0(\text{NaOH}) = 0.1 \text{ M}$, $C_0(\text{TEOA}) = 10 \text{ vol\%}$, $C_{\text{cat}} = 0.5 \text{ g L}^{-1}$; LED light source ($\lambda = 450 \text{ nm}$).

Platinum deposition on the surface of composite samples $\text{Cd}_{1-x}\text{Zn}_x\text{S}/\text{g-C}_3\text{N}_4$, $\text{g-C}_3\text{N}_4$, and $\text{Cd}_{1-x}\text{Zn}_x\text{S}$ ($x = 0.2-0.3$) solid solutions led to a significant increase in activity. However, for photocatalysts prepared according to Scheme 1, when platinum was allocated onto the surface of solid solutions of cadmium and zinc sulfides (Pt/10–50 Cd0.8/CN and Pt/10–50 Cd0.7/CN), the activity of the ternary composite samples did not exceed the activity of platinized single-phase sulfides, such as 1% Pt/ $\text{Cd}_{0.8}\text{Zn}_{0.2}\text{S}$ and 1% Pt/ $\text{Cd}_{0.7}\text{Zn}_{0.3}\text{S}$. This can be explained by the specific surface area of the samples: for $\text{Cd}_{0.8}\text{Zn}_{0.2}\text{S}$ and $\text{Cd}_{0.7}\text{Zn}_{0.3}\text{S}$ solid solutions, the specific surface area was ca. $180 \text{ m}^2 \text{ g}^{-1}$; for $\text{g-C}_3\text{N}_4$, it was about $20 \text{ m}^2 \text{ g}^{-1}$; and for composite samples Pt/10–50 Cd0.8/CN, this value varied from 34 to $67 \text{ m}^2 \text{ g}^{-1}$ (Figure 6c,d). The positive effect due to the formation of heterojunctions between $\text{Cd}_{0.8}\text{Zn}_{0.2}\text{S}$ and $\text{g-C}_3\text{N}_4$ did not compensate for the significant loss of specific surface area. In contrast, a noticeable increase in activity, approximately twofold, compared with the PtCd0.8 and Pt/Cd0.7 samples, was observed for photocatalysts prepared according to Scheme 2 (10–50 Cd0.8/Pt/CN and 10–50 Cd0.7/Pt/CN), for which large, elongated clusters of platinum particles were located at the interface between the $\text{Cd}_{1-x}\text{Zn}_x\text{S}$ and $\text{g-C}_3\text{N}_4$ phases. The highest activity at the level of $2500 \mu\text{mol}$ hydrogen per gram of photocatalyst per hour ($2.1 \mu\text{mol min}^{-1}$) with an apparent quantum efficiency equal to 6.0% at a wavelength of 450 nm was possessed by sample 20% $\text{Cd}_{0.8}\text{Zn}_{0.2}\text{S}/1\% \text{ Pt}/\text{g-C}_3\text{N}_4$ (20 Cd0.8/Pt/CN). This value is comparable with previously published results, as shown in Table 4.

Table 4. Comparison of the results with previously published data.

N	Photocatalyst	Sacrificial Reagent	Light Source	W ₀ , $\mu\text{mol g}^{-1} \text{h}^{-1}$	Ref.
1	3% Pt/2% Na ₂ Fe ₂ Ti ₆ O ₁₆ /g-C ₃ N ₄	10 vol. % TEOA	Xe lamp, $\lambda > 420 \text{ nm}$	389	[51]
2	g-C ₃ N ₄ doped by B	10 vol. % TEOA	Xe lamp, $\lambda > 420 \text{ nm}$	910	[52]
3	1% Pt/W ₁₈ O ₄₉ /g-C ₃ N ₄	10 vol. % TEOA	Xe lamp, $\lambda > 400 \text{ nm}$	912	[53]
4	20% g-C ₃ N ₄ /TiO ₂	10 vol. % TEOA	250 W visible light source	1042	[54]
5	Ru-CoP/g-C ₃ N ₄	10 vol. % TEOA	Xe lamp, $\lambda > 400 \text{ nm}$	1173	[55]
6	9% Ni/porous g-C ₃ N ₄	10 vol. % TEOA	Xe lamp, $\lambda > 420 \text{ nm}$	1274	[56]
7	CoP/B doped g-C ₃ N ₄ nanodots/g-C ₃ N ₄	10 vol. % TEOA	Xe lamp, $\lambda > 420 \text{ nm}$	1333	[57]
8	Ni/N-doped C ₃ N ₄	10 vol. % TEOA	Xe lamp, $\lambda > 420 \text{ nm}$	1507	[58]
9	Ni-Cu/g-C ₃ N ₄	15 vol. % TEOA	5W LED white-light multi-channel	2088	[59]
10	NiS-WO ₃ /g-C ₃ N ₄	15 vol. % TEOA	5 W LED white light, $\lambda \geq 420 \text{ nm}$	2929	[60]
11	40% CdS/4% PdAg/g-C ₃ N ₄	10 vol. % TEOA	Xe lamp, $\lambda > 400 \text{ nm}$	3098	[61]
12	La _x Co _{3-x} O ₄ /g-C ₃ N ₄	10 vol. % TEOA	Xe lamp, $\lambda > 420 \text{ nm}$	3160	[62]
13	1%Pt/20 wt% Cd _{0.8} Zn _{0.2} S/g-C ₃ N ₄	10 vol. % TEOA, 0.1 M NaOH	450-LED	996	This work
14	20 wt% Cd _{0.8} Zn _{0.2} S/1%Pt/g-C ₃ N ₄			2520	

Thus, photocatalysts that are practically identical in chemical composition exhibit quite different activity in the process of photocatalytic production of hydrogen because of the different locations and shapes of the platinum nanoparticles for Pt/20Cd0.8/CN and 20 Cd0.8/Pt/CN samples. We built an energy diagram (Figure 7) for the g-C₃N₄/Cd_{0.8}Zn_{0.2}S system. It was calculated from UV-vis spectroscopy data (Figure 2) that the band gap was 2.8 eV for g-C₃N₄ and 2.4 eV for Cd_{0.8}Zn_{0.2}S. According to the literature data, the CB and VB potentials of g-C₃N₄ were -1.1 and $+1.7$ V vs. NHE, respectively [4,22]; for the Cd_{0.8}Zn_{0.2}S solid solution, CB potential was equal to -0.4 V vs. NHE, and VB level equaled $+2.0$ V vs. NHE [63] (Figure 7). Thus, CB level was more negative for g-C₃N₄, and VB level was more positive for the sulfide solid solution.

**Figure 7.** Scheme of heterojunctions for the photocatalysts Pt/20Cd0.8/CN (a) and 20Cd0.8/Pt/CN (b).

As was discussed above, there are three possible mechanisms for the spatial separation of photogenerated charge carriers in the g-C₃N₄/Cd_{1-x}Zn_xS system: conventional type II heterojunctions, Z-scheme, and S-scheme. However, the Z-scheme photocatalyst is now considered to be misleading by the scientific community [32]. All-solid-state Z-scheme with platinum as a mediator has large restrictions, because if platinum nanoparticles are located between two semiconductors, band bending arises at their interfaces, forming a Schottky barrier, and this Schottky barrier will suppress the electron flow from semiconductors to metal [36]. Additionally, as was shown in this study by TEM with EDX, in the case of both Scheme 1 (Pt/20Cd0.8/CN) and Scheme 2 (20 Cd0.8/Pt/CN), platinum is deposited onto individual semiconductors, Cd_{1-x}Zn_xS or g-C₃N₄, respectively. Thus, we will further discuss the type II heterojunction and S-scheme, and metallic platinum will only be considered as a cocatalyst for the formation of hydrogen.

For photocatalysts synthesized according to Scheme 1, when Cd_{0.8}Zn_{0.2}S particles were deposited on the surface of g-C₃N₄ and Pt nanoparticles were, in turn, deposited onto

the surface of the sulfide solid solution, the formation of hydrogen is most likely localized over sulfide particles, because it is there that the cocatalyst is deposited. The photogenerated electrons likely moved from the CB of $g\text{-C}_3\text{N}_4$ to the CB of $\text{Cd}_{0.8}\text{Zn}_{0.2}\text{S}$ and then to platinum particles, whereas holes from the VB of sulfide solid solution migrated to the VB of $g\text{-C}_3\text{N}_4$ (Figure 7a). Thus, in the case of photocatalyst Pt/20Cd0.8/CN, conventional type II heterojunctions were likely realized. This type of heterojunction has been described for Pt/CdS/ $g\text{-C}_3\text{N}_4$ systems with platinum deposited on CdS nanoparticles [22–24]. Unfortunately, for all samples synthesized according to Scheme 1, no increase in activity in comparison to Pt/ $\text{Cd}_{1-x}\text{Zn}_x\text{S}$ was observed. The obtained results can be explained as follows: when type II heterojunctions appeared in the $\text{Cd}_{1-x}\text{Zn}_x\text{S}/g\text{-C}_3\text{N}_4$ system, the spatial separation of photogenerated electrons and holes was observed; however, the electrons and holes were accumulated in the CB of $\text{Cd}_{1-x}\text{Zn}_x\text{S}$ and the VB of $g\text{-C}_3\text{N}_4$, which possess low reduction and oxidation potentials, respectively [64]. This explains the decrease in photocatalyst activity in the hydrogen evolution from aqueous solutions of TEOA.

For the 20Cd0.8/Pt/CN photocatalyst (Scheme 2), large, elongated clusters of platinum particles were located on the surface of the $g\text{-C}_3\text{N}_4$ phase (Figure 7b). In this case, it is logical to assume that the formation of hydrogen occurs over the $g\text{-C}_3\text{N}_4$ surface. The activity of the 20Cd0.8/Pt/CN photocatalyst was much higher than that of the Pt/20Cd0.8/CN photocatalyst. Moreover, this pattern remained unchanged for all 10–50% $\text{Cd}_{1-x}\text{Zn}_x\text{S}/g\text{-C}_3\text{N}_4$ ($x = 0.2\text{--}0.3$) photocatalysts with 1 wt. % platinum. Additionally, the activity of Scheme 2 composites is much higher than the activity of single-phase platinized 1%Pt/ $\text{Cd}_{1-x}\text{Zn}_x\text{S}$ ($x = 0.2\text{--}0.3$) or 1%Pt/ $g\text{-C}_3\text{N}_4$. It can be assumed that the formation of heterojunctions according to the S-scheme, when electrons remain in CB of $g\text{-C}_3\text{N}_4$ (Figure 7b), whereas electrons from CB of $\text{Cd}_{1-x}\text{Zn}_x\text{S}$ and holes from VB of $g\text{-C}_3\text{N}_4$ recombine, occurs first, and then molecular hydrogen is formed on the platinum cocatalyst particle. This implementation of the process leads to the highest activities in hydrogen production. Additionally, platinum in metallic state and sulfur in S^{2-} state, as was shown by XPS for 20Cd0.8/Pt/CN, can lead to enhanced activity of the Scheme II photocatalysts.

The charge-transfer mechanism in an S-scheme heterojunction can be explained as follows. When $\text{Cd}_{0.8}\text{Zn}_{0.2}\text{S}$ and $g\text{-C}_3\text{N}_4$ are in intimate contact, electrons from CB of $g\text{-C}_3\text{N}_4$ diffuse to CB of $\text{Cd}_{0.8}\text{Zn}_{0.2}\text{S}$, creating an electron depletion layer and an electron accumulation layer near the interface of $g\text{-C}_3\text{N}_4$ and $\text{Cd}_{0.8}\text{Zn}_{0.2}\text{S}$, respectively. Thus, an internal electric field directing from $g\text{-C}_3\text{N}_4$ to $\text{Cd}_{0.8}\text{Zn}_{0.2}\text{S}$ occurs. This internal electric field accelerates the electrons transfer from $\text{Cd}_{0.8}\text{Zn}_{0.2}\text{S}$ to $g\text{-C}_3\text{N}_4$, and hole transfer from $g\text{-C}_3\text{N}_4$ to $\text{Cd}_{0.8}\text{Zn}_{0.2}\text{S}$ as shown in Figure 7b. Additionally, the band bending urges the photogenerated electrons from the CB of $\text{Cd}_{0.8}\text{Zn}_{0.2}\text{S}$ and holes from the VB of $g\text{-C}_3\text{N}_4$ at the interface region. Thus, the photogenerated electrons in the CB of $\text{Cd}_{0.8}\text{Zn}_{0.2}\text{S}$ and holes in the VB of $g\text{-C}_3\text{N}_4$ recombine at the interface under the Coulombic attraction [32].

Thus, on the basis of the above band structure analysis, TEM and XPS analysis of the samples, and enhanced H_2 evolution activity, the formation of S-scheme heterojunctions is more favorable than the type II heterojunction between the $\text{Cd}_{1-x}\text{Zn}_x\text{S}$ and $g\text{-C}_3\text{N}_4$ semiconductors. Note that the synthesis of $\text{Cd}_{1-x}\text{Zn}_x\text{S}/g\text{-C}_3\text{N}_4$ with different locations of platinum particles was conducted for the first time.

Figure 8a presents the normalized PL spectra of C_3N_4 , 1% Pt/ C_3N_4 , Pt/20Cd0.8/CN, 20Cd0.8/Pt/CN, and $\text{Cd}_{0.8}\text{Zn}_{0.2}\text{S}$. The $g\text{-C}_3\text{N}_4$ photocatalyst demonstrated the most intensive photoluminescence; for $\text{Cd}_{0.8}\text{Zn}_{0.2}\text{S}$, photoluminescence was not observed. The obtained spectra for C_3N_4 and 1% Pt/ C_3N_4 were similar in shape but different in intensity. Upon photoexcitation at 380 nm, the emission was centered at 490 nm and may be attributed to $n\text{-}\pi^*$ electronic transitions consisting of lone pairs of N atoms in graphitic carbon nitride [65]. The deposition of Pt onto the surface $g\text{-C}_3\text{N}_4$ photocatalyst led to a decrease in the intensity, at 2.3, which indicated a lower recombination rate of electron-hole pairs in the Pt-containing photocatalyst. The photoluminescence of the ternary composites was also studied. Figure 8a shows that the spectra of Pt/20Cd0.8/CN and 20Cd0.8/Pt/CN were identical in shape; the peak center was at 515 nm. The maximal intensities of Pt/20Cd0.8/CN and

20Cd0.8/Pt/CN were 3.1 and 4 times less than that of g-C₃N₄, respectively. Therefore, the efficiencies of radiative processes in the ternary composites were smaller; these samples can possess higher photocatalytic activity. The photocatalyst prepared according to Scheme 2 also exhibited the lowest photoluminescence intensity.

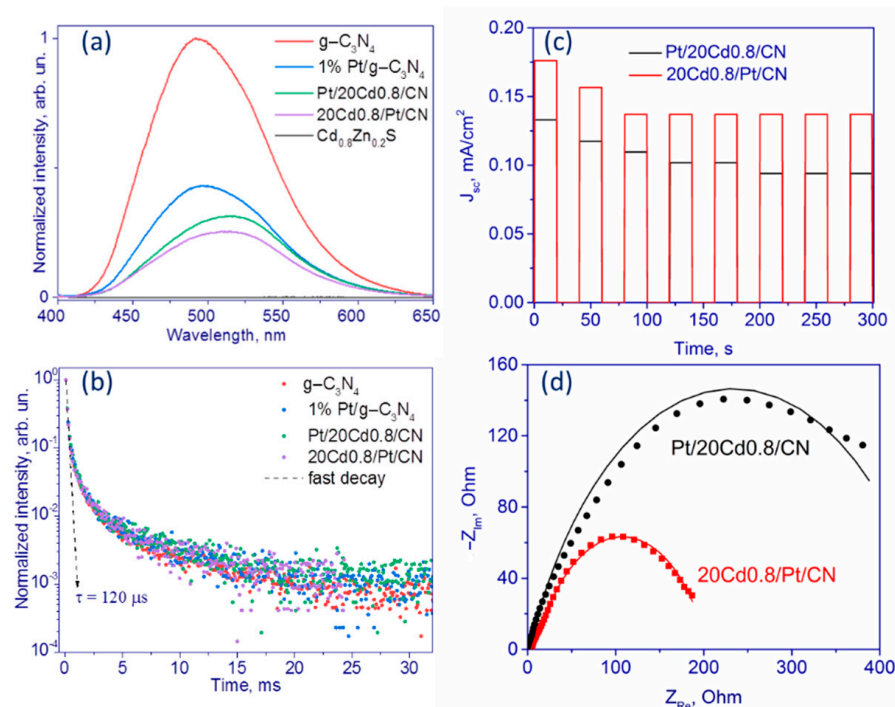


Figure 8. Normalized PL emission spectra of C₃N₄, 1% Pt/C₃N₄, Pt/20Cd0.8/CN, 20Cd0.8/Pt/CN, and Cd_{0.8}Zn_{0.2}S (a); normalized decay curves of PL intensities of the tested samples (b); photocurrent response (c); and EIS (d) of the samples Pt/20Cd0.8/CN (Scheme 1) and 20Cd0.8/Pt/CN (Scheme 2).

Figure 8b shows the decay curves of the PL intensities of the g-C₃N₄-based photocatalysts. All curves were almost identical. Numerical analysis showed that PL intensity decreased by a factor of 100 during 3 ms after the start of measurements. In this case, decay kinetics was nonexponential and could not be represented as a superposition of two or three exponential processes. If we assumed a fast decay of the first-order kinetics, the lifetime of such processes is $\tau = 120 \pm 15 \mu\text{s}$ (see the dashed line in Figure 8b). The nature of the observed behavior in the studied interval of time may be due to the phosphorescent mechanism under the used excitation and the presence of trapping centers of separated charge carriers, which favored photocatalytic hydrogen production.

The photoelectrochemical properties of the samples Pt/20Cd0.8/CN and 20Cd0.8/Pt/CN were tested. Figure 8c shows that both photocatalysts possess typical photocurrent responses during on-off experiments. The photocurrent intensity is slightly higher for the 20Cd0.8/Pt/CN synthesized according to Scheme 2, which indicates more efficient charge separation for this photocatalyst [66]. Additionally, EIS spectra were obtained for these two samples (Figure 8d). Compared with Pt/20Cd0.8/CN photocatalyst, the Nyquist plots of 20Cd0.8/Pt/CN sample exhibit a significantly smaller impedance arc radius. Thus, the electrochemical experiments confirm that construction of the structure of 20Cd0.8/Pt/CN photocatalyst with platinum deposited over g-C₃N₄ surface improves the interface charge separation.

An important aspect of the study of photocatalysts is the investigation of their stability. We tested the activity of the Pt/20Cd0.8/CN and 20Cd0.8/Pt/CN photocatalysts in four consecutive hydrogen evolution runs (Figure 9a). Photocatalyst 20Cd0.8/Pt/CN had greater stability than that of photocatalyst Pt/20Cd0.8/CN. We characterized samples after the hydrogen evolution by the XPS and XRD techniques (Table 3, Figure 9b). Figure 10 shows that the bulk structure of the samples does not undergo any changes. However,

according to XPS data (Table 3) after hydrogen evolution, the following changes took place on the photocatalyst surface:

- Surface ratio $[\text{Cd} + \text{Zn}]/[\text{C}]$ and $[\text{S}]/[\text{C}]$ decreased for both photocatalysts indicating the aggregation of $\text{Cd}_{1-x}\text{Zn}_x\text{S}$ particles; for sample 20Cd0.8/Pt/CN, it was to a lesser extent;
- The $[\text{Pt}]/[\text{C}]$ surface ratio decreased slightly for the Pt/20Cd0.8/CN sample, but this ratio increased threefold for the 20Cd0.8/Pt/CN photocatalysts. This suggests that, in the first case, the metal particles were enlarged, and in the latter, they were dispersed. Please note that the ratio of $[\text{S}]/[\text{C}]$ and $[\text{Cd} + \text{Zn}]/[\text{C}]$ became smaller and simultaneously ratio of $[\text{Pt}]/[\text{Cd} + \text{Zn}]$ became bigger for both samples, that is, the particles of the solid solution of sulfide aggregated, and the size of the platinum particles either practically did not grow (Pt/20Cd0.8/CN), or became smaller (20Cd0.8/Pt/CN).
- Sulfur in the sulfite/sulfate state on the surface completely transformed into sulfide S^{2-} for both samples;
- An increase in the proportion of platinum in zero oxidation state was seen for sample Pt/20Cd0.8/CN; for sample 20Cd0.8/Pt/CN, metallic platinum partially transformed into Pt^{2+} .

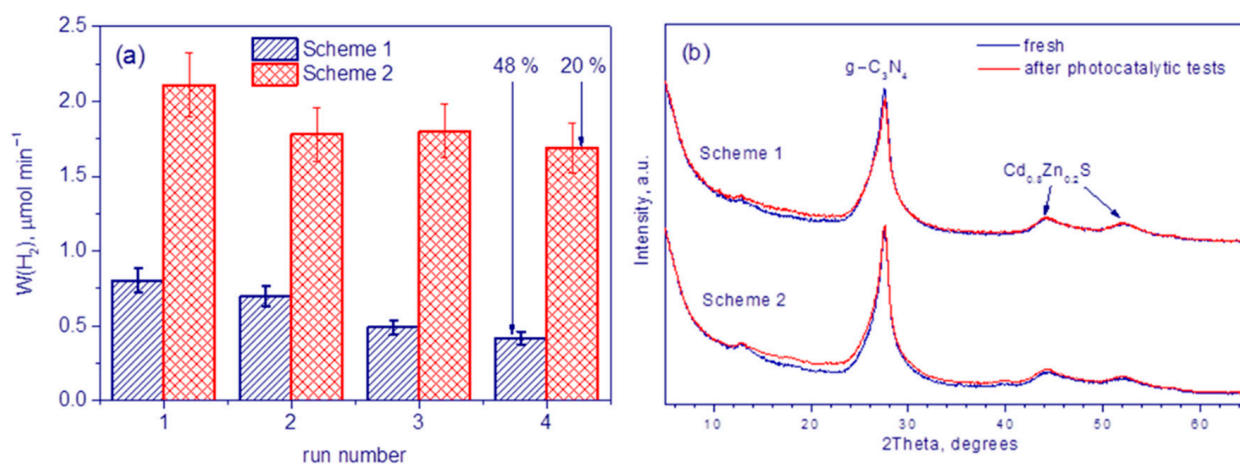


Figure 9. The activity of the photocatalysts Pt/20Cd0.8/CN and 20 Cd0.8/Pt/CN in four 1.5 h consecutive hydrogen evolution runs (a) and XRD patterns of these samples before and after photocatalytic tests (b). Conditions: $C_0(\text{NaOH}) = 0.1 \text{ M}$, $C_0(\text{TEOA}) = 10 \text{ vol\%}$, $C_{\text{cat}} = 0.5 \text{ g L}^{-1}$; LED light source ($\lambda = 450 \text{ nm}$).

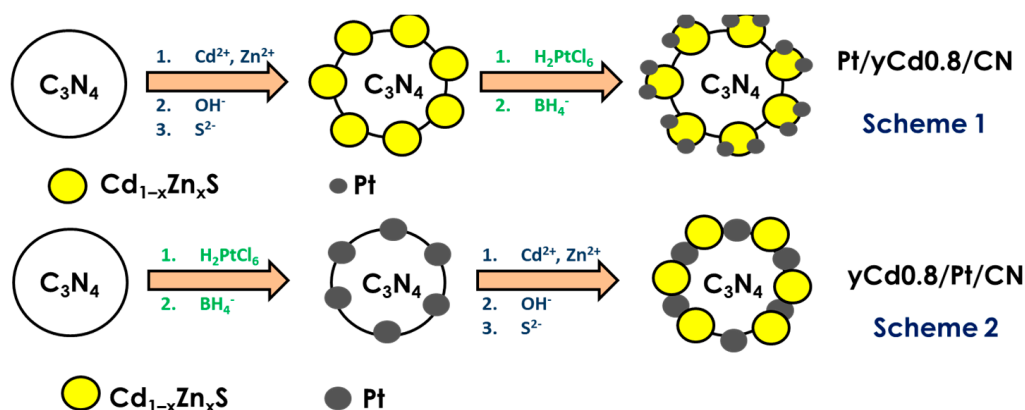


Figure 10. Scheme of the ternary photocatalyst synthesis.

Among these factors, the reduction of Pt^{2+} into metallic platinum, the reduction of SO_x^{2-} anions into S^{2-} , and a decrease in the size of platinum particles had a positive effect on the rate of hydrogen evolution. Regarding the aggregation of both platinum and $\text{Cd}_{1-x}\text{Zn}_x\text{S}$ solid solution particles, this led to photocatalyst deactivation. Based on

these competing factors, the stability of the photocatalyst prepared according to Scheme 2 was much better than the stability of the photocatalyst prepared according to Scheme 1. Thus, the use of synthetic Scheme 2 makes it possible to obtain both active and stable photocatalysts $\text{Cd}_{1-x}\text{Zn}_x\text{S}/\text{Pt}/\text{g-C}_3\text{N}_4$.

3. Materials and Methods

3.1. Photocatalyst Synthesis

3.1.1. Synthesis of $\text{g-C}_3\text{N}_4$

Melamine was chosen as a precursor. Usually, 2 g of the precursor was annealed in a ceramic crucible with a lid at 600 °C with a heating rate of 5 °C/min for 2 h [8]. The obtained $\text{g-C}_3\text{N}_4$ was ground in a mortar to a yellow powder. Platinum (1 wt. %) was deposited on the surface prepared photocatalysts by impregnation with hexachloroplatinic acid followed by reduction with a 2.5-fold excess of sodium borohydride. This method was described in detail earlier [38]. Samples were dried at 50 °C for 4 h after decantation several times.

3.1.2. Synthesis of Photocatalysts Based on $\text{Cd}_{1-x}\text{Zn}_x\text{S}/\text{g-C}_3\text{N}_4$

To prepare the samples $\text{Cd}_{0.7}\text{Zn}_{0.3}\text{S}/\text{g-C}_3\text{N}_4$ and $\text{Cd}_{0.8}\text{Zn}_{0.2}\text{S}/\text{g-C}_3\text{N}_4$ with a certain percentage of $\text{Cd}_{1-x}\text{Zn}_x\text{S}$ (10, 20, and 50%), a proper amount of 0.1 M cadmium chloride and 0.1 M zinc nitrate were added to the suspension of $\text{g-C}_3\text{N}_4$ (Scheme 1) or 1%Pt/ $\text{g-C}_3\text{N}_4$ (Scheme 2), and then the total volume of 0.1 M NaOH equal to the sum of zinc and cadmium chloride volumes was added, and the mixture was stirred for 20 min. Then, a solution of 0.1 M Na_2S with a volume 2.5 times higher than the volume of NaOH was added, and the mixture was stirred for 60 min. The obtained suspension was placed in Teflon beakers, centrifuged, and the precipitate was washed with distilled water. Then the precipitate was decanted and dried for 4 h at 80 °C. The dried sample was ground in a mortar. In the case of Scheme 1, 1 wt. % Pt was deposited on the prepared $\text{Cd}_{1-x}\text{Zn}_x\text{S}/\text{g-C}_3\text{N}_4$ samples by the impregnation method as described above. The composition and the abbreviations of the samples are given in Table 1, the scheme of the synthesis is represented in Figure 10.

3.2. Photocatalysts Characterization

The photocatalysts were characterized by UV–vis optical absorption and luminescence spectroscopy, X-ray diffraction (XRD), X-ray photoelectron spectroscopy (XPS), high-resolution transmission electron microscopy (HRTEM), including the high-angle annular dark-field scanning transmission electron microscopy (HAADF-STEM) technique, N_2 low-temperature adsorption.

The diffuse reflectance UV–vis spectra were obtained using a Shimadzu UV-2501 PC spectrophotometer with an ISR-240A diffuse reflectance unit. XRD patterns were recorded using a Bruker D8 Advance diffractometer in the 2θ range 10° to 80° using the Cu $\text{K}\alpha$ radiation. The mean sizes of crystallites were estimated from the full width at half maximum of corresponding peaks using the Scherrer formula. The specific surface areas of the photocatalysts were obtained from the low-temperature N_2 adsorption–desorption (N_2 adsorption at 77 K) using an ASAP 2400 apparatus.

X-ray photoelectron spectra were measured on a SPECS (Germany) photoelectron spectrometer using a hemispherical PHOIBOS-150-MCD-9 analyzer and FOCUS-500 (Al $\text{K}\alpha$ radiation, $h\nu = 1486.74$ eV, 200 W) monochromator. The binding energy (BE) scale was pre-calibrated using the positions of the peaks of $\text{Au}4f_{7/2}$ (BE = 84.0 eV) and $\text{Cu}2p_{3/2}$ (BE = 932.67 eV) core levels. The samples were loaded onto a conducting double-sided copper scotch. The binding energy of peaks was calibrated by the position of the $\text{C}1s$ peak (BE = 284.8 eV) corresponding to the surface hydrocarbon-like deposits (C–C and C–H bonds).

The structure and microstructure of the photocatalysts were studied by HRTEM using a ThemisZ electron microscope (Thermo Fisher Scientific, Waltham, MA, USA) operated at an accelerating voltage of 200 kV. The microscope was equipped with a corrector of

spherical aberrations, which provided a maximum lattice resolution of 0.06 nm, and a SuperX spectrometer (TFS, Waltham, MA, USA). Images were recorded using a Ceta 16 CCD sensor (Thermo Fisher Scientific, Waltham, MA, USA). For electron microscopy studies, samples were deposited on perforated carbon substrates attached to aluminum grids using an ultrasonic dispersant.

Spectral and kinetic photoluminescent (PL) curves in a millisecond time window were measured on a Perkin Elmer LS55 spectrometer at room temperature. The spectral widths of the slits in the exciting and recording channels were 10 and 20 nm, respectively. PL spectra were recorded in the range 400–650 nm with excitation in the 380 nm band and a scan rate of 60 nm min^{−1}. The experimental spectra were normalized to the maximum PL intensity in the g-C₃N₄ sample. The kinetics of PL decay was recorded in the 490 nm band upon excitation in the 380 nm band. The kinetic dependences were normalized to the maximum value of the PL intensity in each sample.

3.3. Photocatalytic Activity Measurement

The synthesized catalysts were studied in photocatalytic hydrogen evolution from aqueous alkaline triethanolamine (TEOA) solutions [8]. Usually, 50 mg of the photocatalyst was suspended in a solution that contained 10 mL of triethanolamine and 90 mL of 0.11 M NaOH. Then, the suspension was purged with argon for 30 min and illuminated with a 450-LED. The amount of evolved hydrogen was measured on a Khromos GKKh-1000 gas chromatograph (Khromos, Omsk, Russia) equipped with a zeolite column and a thermal conductivity detector. Argon was used as a carrier gas. The photocatalytic activity of the samples was estimated as the hydrogen evolution rate (μmol min^{−1}). The apparent quantum efficiency (AQE) was calculated by the following formula:

$$AQE = \frac{W}{N_{ph}} \times 100\%, \quad (1)$$

where W —reaction rate (μmol min^{−1}), N_{ph} —photon flux (μEinstein min^{−1}). For all experiments, $N_{ph} = 34 \mu\text{Einstein min}^{-1}$.

3.4. Photoelectrochemical Experiments

Photoelectrochemical experiments were conducted using a two-electrode cell. The working electrode was FTO with the photocatalyst deposited by the drop-casting method. The counter electrode was Cu₂S/brass, the electrolyte was a solution consisting of 1 M Na₂S_n and 0.1 M NaCl. Photoelectrochemical characteristics were obtained using a potentiostat–galvanostat P-45X (Electrochemical Instruments, Chernogolovka, Russia). The current–time curves were registered at 0 V. The impedance data were recorded over a frequency range of 0.8 to 10⁵ Hz with an amplitude of 10 mV at 0.2 V. The light source was 450-LED, which was used for the photocatalytic tests. ×

4. Conclusions

In this work, a new technique for constructing efficient Cd_{1−x}Zn_xS/Pt/g-C₃N₄ heterojunctions was proposed. Two groups of ternary photocatalysts based on platinized 10–50 wt. % Cd_{1−x}Zn_xS/g-C₃N₄ ($x = 0.2–0.3$) were synthesized. It was shown for the first time that, by changing the order of platinum deposition, one can obtain two types of photocatalysts, Pt/Cd_{1−x}Zn_xS/g-C₃N₄ and Cd_{1−x}Zn_xS/Pt/g-C₃N₄, with a different structure: in the first case, small platinum particles are deposited onto the surface of the solid solution of cadmium and zinc sulfides; in the latter case, enlarged platinum clusters are located over the surface of graphitic carbon nitride.

The rate of photocatalytic hydrogen production under visible light was much higher in the case of using photocatalysts of the second type, Cd_{1−x}Zn_xS/1 wt. % Pt/g-C₃N₄, in comparison to photocatalysts of the first type, 1 wt. % Pt/Cd_{1−x}Zn_xS/g-C₃N₄ with a similar bulk structure of Cd_{1−x}Zn_xS and g-C₃N₄ and equal mass fractions of components.

Analysis of the band-gap structure of ternary samples, and TEM and XPS analyses showed that, for more active photocatalysts, the mechanism of interphase heterojunctions according to the S-scheme is most likely realized, while photocatalysts with low activity are characterized by type II heterojunctions. Moreover, S-scheme photocatalysts have greater stability than type II heterojunction photocatalysts do. The highest activity, $2.5 \text{ mmol H}_2 \text{ g}^{-1} \text{ h}^{-1}$, with an apparent quantum efficiency equal to 6.0% at a wavelength of 450 nm was performed by sample 20% $\text{Cd}_{0.8}\text{Zn}_{0.2}\text{S}/1\% \text{ Pt/g-C}_3\text{N}_4$. The synthesis of $\text{Cd}_{1-x}\text{Zn}_x\text{S/g-C}_3\text{N}_4$ with different locations of platinum particles and the assessment of their photocatalytic properties was carried out for the first time.

Supplementary Materials: The following are available online at <https://www.mdpi.com/article/10.3390/catal11111340/s1>, Table S1: EDX data of the photocatalyst 20Cd0.8/Pt/CN; domain with predominated g-C₃N₄ content; Table S2: EDX data of the photocatalyst 20Cd0.8/Pt/CN; domain with predominated g-C₃N₄ content; Table S3: EDX data of the photocatalyst 20Cd0.8/Pt/CN; domain with g-C₃N₄ and Cd_{0.8}Zn_{0.2}S; Table S4: EDX data of the photocatalyst 20Cd0.8/Pt/CN; domain with g-C₃N₄ and Cd_{0.8}Zn_{0.2}S.

Author Contributions: Conceptualization, A.V.Z.; validation, A.V.Z.; formal analysis, I.P.P., S.V.C. and A.V.B.; investigation, D.V.M., E.Y.G. and I.A.W.; data curation, D.V.M., A.S.V., I.P.P., S.V.C. and A.V.B.; writing—original draft preparation, A.V.Z., D.V.M. and E.A.K.; visualization, A.V.Z., D.V.M., E.Y.G. and A.S.V.; supervision, I.A.W. and E.A.K.; project administration, E.A.K.; funding acquisition, E.A.K. All authors have read and agreed to the published version of the manuscript.

Funding: This work was supported by the Ministry of Science and Higher Education of the Russian Federation within the governmental order for Boreskov Institute of Catalysis (project AAAA-A21-121011390009-1) and was also funded by the Russian Foundation for Basic Research (project No. 20-33-70086). A.S.V. and I.A.W. thank Minobrnauki research project FEUZ-2020-0059 for financial support.

Data Availability Statement: The data presented in this study are available on request from the corresponding author.

Acknowledgments: The authors are grateful to T.V. Larina for DRS analysis. The studies were conducted using the equipment of the Center of Collective Use “National Center of Catalyst Research”.

Conflicts of Interest: The authors declare no conflict of interest.

References

1. Domen, K.; Hara, M.; Kondo, J.; Takata, T.; Kudo, A.; Kobayashi, H.; Inoue, Y. New aspects of heterogeneous photocatalysts for water decomposition. *Korean J. Chem. Eng.* **2001**, *18*, 862–866. [\[CrossRef\]](#)
2. Fujishima, A.; Honda, K. Electrochemical Photolysis of Water at a Semiconductor Electrode. *Nature* **1972**, *238*, 37–38. [\[CrossRef\]](#) [\[PubMed\]](#)
3. Wang, X.; Maeda, K.; Thomas, A.; Takanabe, K.; Xin, G.; Carlsson, J.M.; Domen, K.; Antonietti, M. A metal-free polymeric photocatalyst for hydrogen production from water under visible light. *Nat. Mater.* **2009**, *8*, 76–80. [\[CrossRef\]](#) [\[PubMed\]](#)
4. Ye, S.; Wang, R.; Wu, M.-Z.; Yuan, Y.-P. A review on g-C₃N₄ for photocatalytic water splitting and CO₂ reduction. *Appl. Surf. Sci.* **2015**, *358*, 15–27. [\[CrossRef\]](#)
5. Madhusudan, P.; Shi, R.; Xiang, S.; Jin, M.; Chandrashekar, B.N.; Wang, J.; Wang, W.; Peng, O.; Amini, A.; Cheng, C. Construction of highly efficient Z-scheme $\text{ZnxCd}_{1-x}\text{S}/\text{Au@g-C}_3\text{N}_4$ ternary heterojunction composite for visible-light-driven photocatalytic reduction of CO₂ to solar fuel. *Appl. Catal. B Environ.* **2021**, *282*, 119600. [\[CrossRef\]](#)
6. Safaei, J.; Mohamed, N.A.; Noh, M.F.M.; Soh, M.F.; Ludin, N.A.; Ibrahim, M.A.; Isahak, W.N.R.W.; Teridi, M.A.M. Graphitic carbon nitride (g-C₃N₄) electrodes for energy conversion and storage: A review on photoelectrochemical water splitting, solar cells and supercapacitors. *J. Mater. Chem. A* **2018**, *6*, 22346–22380. [\[CrossRef\]](#)
7. Kumar, P.; Boukherroub, R.; Shankar, K. Sunlight-driven water-splitting using two-dimensional carbon based semiconductors. *J. Mater. Chem. A* **2018**, *6*, 12876–12931. [\[CrossRef\]](#)
8. Zhurenok, A.V.; Larina, T.V.; Markovskaya, D.V.; Cherepanova, S.V.; Mel’Gunova, E.A.; Kozlova, E.A. Synthesis of graphitic carbon nitride-based photocatalysts for hydrogen evolution under visible light. *Mendeleev Commun.* **2021**, *31*, 157–159. [\[CrossRef\]](#)
9. Kozlova, E.; Parmon, V.N. Heterogeneous semiconductor photocatalysts for hydrogen production from aqueous solutions of electron donors. *Russ. Chem. Rev.* **2017**, *86*, 870–906. [\[CrossRef\]](#)
10. Ismail, A.A.; Bahnemann, D.W. Photochemical splitting of water for hydrogen production by photocatalysis: A review. *Sol. Energy Mater. Sol. Cells* **2014**, *128*, 85–101. [\[CrossRef\]](#)

11. Li, X.; Xiong, J.; Gao, X.; Huang, J.; Feng, Z.; Chen, Z.; Zhu, Y. Recent advances in 3D g-C₃N₄ composite photocatalysts for photocatalytic water splitting, degradation of pollutants and CO₂ reduction. *J. Alloys Compd.* **2019**, *802*, 196–209. [\[CrossRef\]](#)
12. Vorontsov, A.V.; Kozlova, E.; Besov, A.S.; Kozlov, D.V.; Kiselev, S.A.; Safatov, A. Photocatalysis: Light energy conversion for the oxidation, disinfection, and decomposition of water. *Kinet. Catal.* **2010**, *51*, 801–808. [\[CrossRef\]](#)
13. Solakidou, M.; Giannakas, A.; Georgiou, Y.; Boukos, N.; Louloudi, M.; Deligiannakis, Y. Efficient photocatalytic water-splitting performance by ternary CdS/Pt-N-TiO₂ and CdS/Pt-N,F-TiO₂: Interplay between CdS photo corrosion and TiO₂-dopping. *Appl. Catal. B Environ.* **2019**, *254*, 194–205. [\[CrossRef\]](#)
14. He, H.; Cao, J.; Guo, M.; Lin, H.; Zhang, J.; Chen, Y.; Chen, S. Distinctive ternary CdS/Ni₂P/g-C₃N₄ composite for overall water splitting: Ni₂P accelerating separation of photocarriers. *Appl. Catal. B Environ.* **2019**, *249*, 246–256. [\[CrossRef\]](#)
15. Yan, J.; Wu, H.; Chen, H.; Zhang, Y.; Zhang, F.; Liu, S.F. Fabrication of TiO₂/C₃N₄ heterostructure for enhanced photocatalytic Z-scheme overall water splitting. *Appl. Catal. B Environ.* **2016**, *191*, 130–137. [\[CrossRef\]](#)
16. Hussain, M.Z.; van der Linden, B.; Yang, Z.; Jia, Q.; Chang, H.; Fischer, R.A.; Kapteijn, F.; Zhu, Y.; Xia, Y. Bimetal–organic framework derived multi-heterostructured TiO₂/Cu₂O/C nanocomposites with superior photocatalytic H₂ generation performance. *J. Mater. Chem. A* **2021**, *9*, 4103–4116. [\[CrossRef\]](#)
17. Zhu, C.; Wei, T.; Wei, Y.; Wang, L.; Lu, M.; Yuan, Y.-P.; Yin, L.; Huang, L. Unravelling intramolecular charge transfer in donor–acceptor structured g-C₃N₄ for superior photocatalytic hydrogen evolution. *J. Mater. Chem. A* **2021**, *9*, 1207–1212. [\[CrossRef\]](#)
18. Qin, Z.; Fang, W.; Liu, J.; Wei, Z.; Jiang, Z.; Shangguan, W. Zinc-doped g-C₃N₄/BiVO₄ as a Z-scheme photocatalyst system for water splitting under visible light. *Chin. J. Catal.* **2018**, *39*, 472–478. [\[CrossRef\]](#)
19. Guo, F.; Shi, W.; Zhu, C.; Li, H.; Kang, Z. CoO and g-C₃N₄ complement each other for highly efficient overall water splitting under visible light. *Appl. Catal. B Environ.* **2018**, *226*, 412–420. [\[CrossRef\]](#)
20. Zhao, H.; Ding, X.; Zhang, B.; Li, Y.; Wang, C. Enhanced photocatalytic hydrogen evolution along with byproducts suppressing over Z-scheme Cd_xZn_{1-x}S/Au/g-C₃N₄ photocatalysts under visible light. *Sci. Bull.* **2017**, *62*, 602–609. [\[CrossRef\]](#)
21. Ma, X.; Jiang, Q.; Guo, W.; Zheng, M.; Xu, W.; Ma, F.; Hou, B. Fabrication of g-C₃N₄/Au/CdZnS Z-scheme photocatalyst to enhance photocatalysis performance. *RSC Adv.* **2016**, *6*, 28263–28269. [\[CrossRef\]](#)
22. Cao, S.; Yuan, Y.-P.; Fang, J.; Shahjamali, M.M.; Boey, F.Y.; Barber, J.; Loo, S.C.J.; Xue, C. In-situ growth of CdS quantum dots on g-C₃N₄ nanosheets for highly efficient photocatalytic hydrogen generation under visible light irradiation. *Int. J. Hydrogen Energy* **2013**, *38*, 1258–1266. [\[CrossRef\]](#)
23. Zhou, X.; Fang, Y.; Cai, X.; Zhang, S.; Yang, S.; Wang, H.; Zhong, X.; Fang, Y. In Situ Photodeposited Construction of Pt–CdS/g-C₃N₄–MnO_x Composite Photocatalyst for Efficient Visible-Light-Driven Overall Water Splitting. *ACS Appl. Mater. Interfaces* **2020**, *12*, 20579–20588. [\[CrossRef\]](#)
24. Pan, J.; Wang, P.; Wang, P.; Yu, Q.; Wang, J.; Song, C.; Zheng, Y.; Li, C. The photocatalytic overall water splitting hydrogen production of g-C₃N₄/CdS hollow core–shell heterojunction via the HER/OER matching of Pt/MnO_x. *Chem. Eng. J.* **2021**, *405*, 126622. [\[CrossRef\]](#)
25. Chen, L.; Xu, Y.; Chen, B. In situ photochemical fabrication of CdS/g-C₃N₄ nanocomposites with high performance for hydrogen evolution under visible light. *Appl. Catal. B Environ.* **2019**, *256*, 117848. [\[CrossRef\]](#)
26. Li, W.; Feng, C.; Dai, S.; Yue, J.; Hua, F.; Hou, H. Fabrication of sulfur-doped g-C₃N₄/Au/CdS Z-scheme photocatalyst to improve the photocatalytic performance under visible light. *Appl. Catal. B Environ.* **2015**, *168–169*, 465–471. [\[CrossRef\]](#)
27. Hu, J.; Yu, C.; Zhai, C.; Hu, S.; Wang, Y.; Fu, N.; Zeng, L.; Zhu, M. 2D/1D heterostructure of g-C₃N₄ nanosheets/CdS nanowires as effective photo-activated support for photoelectrocatalytic oxidation of methanol. *Catal. Today* **2018**, *315*, 36–45. [\[CrossRef\]](#)
28. Kozlova, E.A.; Lyulyukin, M.N.; Markovskaya, D.V.; Selishchev, D.S.; Cherepanova, S.V.; Kozlov, D.V. Synthesis of Cd_{1-x}Zn_xS photocatalysts for gas-phase CO₂ reduction under visible light. *Photochem. Photobiol. Sci.* **2019**, *18*, 871–877. [\[CrossRef\]](#) [\[PubMed\]](#)
29. Rhimi, B.; Wang, C.; Bahnemann, D.W. Latest progress in g-C₃N₄ based heterojunctions for hydrogen production via photocatalytic water splitting: A mini review. *J. Phys. Energy* **2020**, *2*, 042003. [\[CrossRef\]](#)
30. Zhu, Y.; Cui, Y.; Xiao, B.; Ou-Yang, J.; Li, H.; Chen, Z. Z-scheme 2D/2D g-C₃N₄/SnO₂ heterojunction for enhanced visible-light photocatalytic H₂ evolution and degradation of ciprofloxacin. *Mater. Sci. Semicond. Process.* **2021**, *129*, 105767. [\[CrossRef\]](#)
31. Zhao, D.; Wang, Y.; Dong, C.-L.; Huang, Y.-C.; Chen, J.; Xue, F.; Shen, S.; Guo, L. Boron-doped nitrogen-deficient carbon nitride-based Z-scheme heterostructures for photocatalytic overall water splitting. *Nat. Energy* **2021**, *6*, 388–397. [\[CrossRef\]](#)
32. Xu, Q.; Zhang, L.; Cheng, B.; Fan, J.; Yu, J. S-Scheme Heterojunction Photocatalyst. *J. Chem.* **2020**, *6*, 1543–1559. [\[CrossRef\]](#)
33. Fu, J.; Yu, J.; Jiang, C.; Cheng, B. g-C₃N₄-Based Heterostructured Photocatalysts. *Adv. Energy Mater.* **2018**, *8*, 1701503. [\[CrossRef\]](#)
34. Zheng, D.; Pang, C.; Wang, X. The function-led design of Z-scheme photocatalytic systems based on hollow carbon nitride semiconductors. *Chem. Commun.* **2015**, *51*, 17467–17470. [\[CrossRef\]](#)
35. He, Y.; Zhang, L.; Teng, B.; Fan, M. New Application of Z-Scheme Ag₃PO₄/g-C₃N₄ Composite in Converting CO₂ to Fuel. *Environ. Sci. Technol.* **2015**, *49*, 649–656. [\[CrossRef\]](#)
36. Di, T.; Xu, Q.; Ho, W.; Tang, H.; Xiang, Q.; Yu, J. Review on Metal Sulphide-based Z-scheme Photocatalysts. *ChemCatChem* **2019**, *11*, 1394–1411. [\[CrossRef\]](#)
37. Yang, J.; Wang, D.; Han, H.; Li, C. Roles of Cocatalysts in Photocatalysis and Photoelectrocatalysis. *Acc. Chem. Res.* **2013**, *46*, 1900–1909. [\[CrossRef\]](#)

38. Vasilchenko, D.; Topchiyan, P.; Tsygankova, A.; Asanova, T.; Kolesov, B.; Bukhtiyarov, A.; Kurenkova, A.; Kozlova, E. Photoinduced Deposition of Platinum from $(\text{Bu}_4\text{N})_2[\text{Pt}(\text{NO}_3)_6]$ for a Low Pt-Loading Pt/TiO₂ Hydrogen Photogeneration Catalyst. *ACS Appl. Mater. Interfaces* **2020**, *12*, 48631–48641. [CrossRef] [PubMed]
39. Ran, Y.; Zhang, Y.; Fang, Y.; Zhang, W.; Cui, Y.; Yu, X.; Lan, H.; An, X. Assembly synthesis of puff pastry-like g-C₃N₄/CdS heterostructure as S-junctions for efficient photocatalytic water splitting. *Chem. Eng. J.* **2021**. [CrossRef]
40. Zhang, Y.; Chai, C.; Zhang, X.; Liu, J.; Duan, D.; Fan, C.; Wang, Y. Construction of Pt-decorated g-C₃N₄/Bi₂WO₆ Z-scheme composite with superior solar photocatalytic activity toward rhodamine B degradation. *Inorg. Chem. Commun.* **2019**, *100*, 81–91. [CrossRef]
41. Silva, G.S.T.; Carvalho, K.T.G.; Lopes, O.; Ribeiro, C. g-C₃N₄/Nb₂O₅ heterostructures tailored by sonochemical synthesis: Enhanced photocatalytic performance in oxidation of emerging pollutants driven by visible radiation. *Appl. Catal. B Environ.* **2017**, *216*, 70–79. [CrossRef]
42. He, Y.; Wang, Y.; Zhang, L.; Teng, B.; Fan, M. High-efficiency conversion of CO₂ to fuel over ZnO/g-C₃N₄ photocatalyst. *Appl. Catal. B Environ.* **2015**, *168–169*, 1–8. [CrossRef]
43. Huang, Z.; Chen, H.; Zhao, L.; Fang, W.; He, X.; Li, W.; Tian, P. In situ inducing electron-donating and electron-withdrawing groups in carbon nitride by one-step NH₄Cl-assisted route: A strategy for high solar hydrogen production efficiency. *Environ. Int.* **2019**, *126*, 289–297. [CrossRef] [PubMed]
44. Yang, M.; Shrestha, N.K.; Schmuki, P. Self-organized CdS microstructures by anodization of Cd in chloride containing Na₂S solution. *Electrochimica Acta* **2009**, *55*, 7766–7771. [CrossRef]
45. Wang, Q.; Zhou, J.; Zhang, J.; Zhu, H.; Feng, Y.; Jin, J. Effect of ceria doping on catalytic activity and SO₂ resistance of MnO_x/TiO₂ catalysts for selective catalytic reduction of NO with NH₃ at low temperature. *Aerosol Air Qual. Res.* **2020**, *10*, 935–939. [CrossRef]
46. Steinrück, H.-P.; Pesty, F.; Zhang, L.; Madey, T.E. Ultrathin films of Pt on TiO₂(110): Growth and chemisorption-induced surfactant effects. *Phys. Rev. B* **1995**, *51*, 2427–2439. [CrossRef]
47. Bancroft, G.M.; Adams, I.; Coatsworth, L.L.; Bennewitz, C.D.; Brown, J.D.; Westwood, W.D. ESCA study of sputtered platinum films. *Anal. Chem.* **1975**, *47*, 586–588. [CrossRef]
48. Kurenkova, A.Y.; Markovskaya, D.V.; Gerasimov, E.Y.; Prosvirin, I.P.; Cherepanova, S.V.; Kozlova, E.A. New insights into the mechanism of photocatalytic hydrogen evolution from aqueous solutions of saccharides over CdS-based photocatalysts under visible light. *Int. J. Hydrogen Energy* **2020**, *45*, 30165–30177. [CrossRef]
49. Kiss, J.; Kukovecz, A.; Kónya, Z. Beyond Nanoparticles: The Role of Sub-nanosized Metal Species in Heterogeneous Catalysis. *Catal. Lett.* **2019**, *149*, 1441–1454. [CrossRef]
50. Pellegrin, Y.; Odobel, F. Sacrificial electron donor reagents for solar fuel production. *Comptes Rendus Chim.* **2017**, *20*, 283–295. [CrossRef]
51. Guo, Z.-Q.; Chen, Q.-W.; Zhou, J.-P. Na₂Fe₂Ti₆O₁₆ as a hybrid co-catalyst on g-C₃N₄ to enhance the photocatalytic hydrogen evolution under visible light illumination. *Appl. Surf. Sci.* **2020**, *509*, 145357. [CrossRef]
52. Mishra, B.P.; Babu, P.; Parida, K. Phosphorous, boron and sulfur doped g-C₃N₄ nanosheet: Synthesis, characterization, and comparative study towards photocatalytic hydrogen generation. *Mater. Today Proc.* **2021**, *35*, 258–262. [CrossRef]
53. Li, A.; Peng, Z.; Fu, X. Exfoliated, mesoporous W₁₈O₄₉/g-C₃N₄ composites for efficient photocatalytic H₂ evolution. *Solid State Sci.* **2020**, *106*, 106298. [CrossRef]
54. Alcudia-Ramos, M.; Fuentez-Torres, M.; Ortiz-Chi, F.; Espinosa-González, C.; Hernandez-Como, N.; Garcia-Zaleta, D.S.; Kesarla, M.; Torres, J.G.T.; Collins-Martínez, V.; Godavarthi, S. Fabrication of g-C₃N₄/TiO₂ heterojunction composite for enhanced photocatalytic hydrogen production. *Ceram. Int.* **2020**, *46*, 38–45. [CrossRef]
55. Meng, S.; An, P.; Chen, L.; Sun, S.; Xie, Z.; Chen, M.; Jiang, D. Integrating Ru-modulated CoP nanosheets binary co-catalyst with 2D g-C₃N₄ nanosheets for enhanced photocatalytic hydrogen evolution activity. *J. Colloid Interface Sci.* **2021**, *585*, 108–117. [CrossRef]
56. Deng, P.; Hong, W.; Cheng, Z.; Zhang, L.; Hou, Y. Facile fabrication of nickel/porous g-C₃N₄ by using carbon dot as template for enhanced photocatalytic hydrogen production. *Int. J. Hydrogen Energy* **2020**, *45*, 33543–33551. [CrossRef]
57. Li, H.; Zhao, J.; Geng, Y.; Li, Z.; Li, Y.; Wang, J. Construction of CoP/B doped g-C₃N₄ nanodots/g-C₃N₄ nanosheets ternary catalysts for enhanced photocatalytic hydrogen production performance. *Appl. Surf. Sci.* **2019**, *496*, 143738. [CrossRef]
58. Deng, P.; Gan, M.; Zhang, X.; Li, Z.; Hou, Y. Non-noble-metal Ni nanoparticles modified N-doped g-C₃N₄ for efficient photocatalytic hydrogen evolution. *Int. J. Hydrogen Energy* **2019**, *44*, 30084–30092. [CrossRef]
59. Jin, Z.; Zhang, L. Performance of Ni-Cu bimetallic co-catalyst g-C₃N₄ nanosheets for improving hydrogen evolution. *J. Mater. Sci. Technol.* **2020**, *49*, 144–156. [CrossRef]
60. Zhang, L.; Hao, X.; Li, Y.; Jin, Z. Performance of WO₃/g-C₃N₄ heterojunction composite boosting with NiS for photocatalytic hydrogen evolution. *Appl. Surf. Sci.* **2020**, *499*, 143862. [CrossRef]
61. Gao, J.; Zhang, F.; Xue, H.; Zhang, L.; Peng, Y.; Li, X.; Gao, Y.; Li, N.; Lei, G. In-situ synthesis of novel ternary CdS/PdAg/g-C₃N₄ hybrid photocatalyst with significantly enhanced hydrogen production activity and catalytic mechanism exploration. *Appl. Catal. B Environ.* **2021**, *281*, 119509. [CrossRef]
62. Xu, J.; Yu, H.; Guo, H. Synthesis and behaviors of g-C₃N₄ coupled with La_xCo_{3-x}O₄ nanocomposite for improved photocatalytic activity and stability under visible light. *Mater. Res. Bull.* **2018**, *105*, 342–348. [CrossRef]

-
63. Jing, D.; Guo, L.; Zhao, L.; Zhang, X.; Liu, H.; Li, M.; Shen, S.; Liu, G.; Hu, X.; Zhang, X. Efficient solar hydrogen production by photocatalytic water splitting: From fundamental study to pilot demonstration. *Int. J. Hydrogen Energy* **2010**, *35*, 7087–7097. [[CrossRef](#)]
 64. Gusain, R.; Kumar, P.; Sharma, O.P.; Jain, S.L.; Khatri, O.P. Reduced graphene oxide–CuO nanocomposites for photocatalytic conversion of CO₂ into methanol under visible light irradiation. *Appl. Catal. B Environ.* **2016**, *181*, 352–362. [[CrossRef](#)]
 65. Liu, Y.; Zhang, X.; Wang, J.; Yang, P. Preparation of luminescent graphitic C₃N₄ NS and their composites with RGO for property controlling. *RSC Adv.* **2016**, *6*, 112581–112588. [[CrossRef](#)]
 66. Markovskaya, D.V.; Zhurenok, A.V.; Cherepanova, S.V.; Kozlova, E.A. Solid solutions of CdS and ZnS: Comparing photocatalytic activity and photocurrent generation. *Appl. Surf. Sci. Adv.* **2021**, *4*, 100076. [[CrossRef](#)]